Master's thesis

NTNU
Norwegian University of Science and Technology
Faculty of Natural Sciences
Department of Physics

Henrik Roven

A DFT analysis on copper based metallic-organic decomposition ink

Master's thesis in MSc in Physics
Supervisor: Jaakko Akola
January 2020

NTNU
Norwegian University of
Science and Technology

Henrik Roven

A DFT analysis on copper based metallic-organic decomposition ink

Master's thesis in MSc in Physics
Supervisor: Jaakko Akola
January 2020

Norwegian University of Science and Technology
Faculty of Natural Sciences
Department of Physics

NTNU
Norwegian University of
Science and Technology

Summary

A new generation of copper based electronic inks have recently emerged that decomposes to metallic copper under thermal heating. The inks are based on copper formate complexes in a +2 oxidation state, whereupon heating reduces to an intermediate +1 oxidation state, before finally decomposing to metallic copper. Recently it was shown that the decomposition temperature of the copper complex is correlated to the molecular structure of both the oxidation states and the stability of the intermediate structure. To that end, density functional theory has been used to investigate the structure and oxidation of three copper complexes in both the gas phase and as crystalline solid. The strength of the copper formate bond was investigated under stretching, while continuously monitoring the oxidation state with the DDEC6 atomic population analysis. The trend observed was that the complex with stronger bond had the higher reduction temperature. Furthermore, calculated infrared spectra of the crystal structures $Cu[HCOO]_2$ and $Cu(C_5H_5N)[HCOO]_2$ are reported. In addition molecular dynamics have been performed on the crystal $Cu[HCOO]_2$ where the temperature, particle number and volume where constrained. The density functional theory and molecular dynamics calculations are done with the exchange correlation functional PBE.

Sammendrag

En ny generasjon av kobber basert elektronisk blekk har blitt nylig utviklet som dekomponeres til metallisk kobber under varme. Blekkene er basert på kobber format komplekser i en +2 oksidasjonstall, som reduseres til en mellomliggende +1 oksidasjonstilstand, før den endelig dekomponeres til metallisk kobber. Nylig ble det vist at dekomponeringstemperaturen av kobber komplekset er korrelert til molekylær strukturen av begge oksidasjonstilstandene og stabiliteten av den mellomliggende oksidasjonstilstanden. Det har derfor blitt brukt tetthetsfunksjonal teori for å studere strukturen og oksidasjonen til tre kobber komplekser i både gas fase og som krystallinsk materiale. Styrken på kobber format bindingen ble undersøkt under tøyning, og samtidig overvåket oksidasjonstilstanden med DDEC6 atomistisk populasjons analyse. Trenden som ble observert var at komplekser med en sterk binding hadde høyere reduseringstemperatur. Videre blir det presentert infrarød spektrum av krystallstrukturene Cu[HCOO]2 and Cu(C5H5N)[HCOO]2. I tillegg ble molekylærdynamikk brukt på krystallet Cu[HCOO]2 ved konstante temperaturer, partikkel antall og volum. Tetthetsfunksjonals teorien og molekylærdynamikken ble gjort med exchange-correlation funksjonalen PBE.

Preface

As a part of the master program in Physics at Norwegian University of Science and Technology (NTNU), it is mandatory to write a master thesis. During the spring and fall of 2019, I performed all work and wrote my thesis. The idea behind this project is from my supervisor Professor Jaakko Akolo, who also made research on this topic possible.

Acknowledgements

I would like to thank Professor Jaakko Akola for his guidance throughout this thesis work. I would also like to thank my family and friends for their support and encouragement.

Table of Contents

List of Tables

List of Figures

Chapter 1

Introduction

All electronic devices require a conductive structure between its electronic components. In electronic science there is an emerging technology, which aims to manufacture the conductive structure based on conventional printing techniques. Traditionally, the printing circuit board industry make use of lithography technology to manufacture the circuits [1]. This is a complex and time consuming method requiring expensive facilities [2]. Being able to use printing techniques, e.g. inkjet printing, screen printing, with a metallic ink instead, allows for a faster, versatile method where one can change the design with ease from one production batch to another.

For the development of flexible electronics there is an additional demand that the inks should be curable at low temperatures, to prevent deformation of the flexible substrate. In general, the inks should be nontoxic, stable, compatible with the printing technique, and inexpensive [3]. Silver has been the most important and successful printable metal [4], due to its high conductivity and chemical inertness. However, as copper (Cu) is significantly cheaper with similar conductivity, there is a strong motivation to develop Cu based inks. One of the challenges to overcome using Cu based inks is that Cu oxidizes in ambient conditions, which can deteriorate the conductivity. In fact there exists already an ink formulation, based on Cu nanoparticles which is already commercially available [2]. Here the Cu nanoparticles are in their reduced state, dispersed in a solution and surrounded by a stabilizing agent and other additives. This is to achieve a stable ink with regards to aggregation, precipitation and oxidation. In order to have a conductive layer one has to remove the agents surrounding the Cu particles by heating and sintering, i.e. bonding the Cu particles together [5].

Alternatively the Cu ink can be designed such that each Cu atom is in a +2 oxidation state (Cu(II)) in solution, with organic anions as ligands. The organic anions, for instance formate $[HCOO]^{-1}$, will upon heating decompose to gaseous products, such as carbon dioxide (CO_2), molecular hydrogen (H_2) and water (H_2O), while the excess electrons are transferred to the Cu ions and thus reducing the Cu ion. To assure that the ink is stable, the Cu ions are typically coordinated to amine ligands. Moreover, these coordinating ligands stabilize the Cu ions in solution, reduce oxidation under thermal curing and lower

the decomposition temperature. Thermal curing of the ink in an inert atmosphere will result in the ligands and organic anions decompose or evaporate away completely, and consequently only metallic Cu will remain. Cu inks formulated in this manner can be categorized as a *metal-organic decomposition* (MOD) ink. The working principle of Cu MOD ink is illustrated in Figure 1.1.

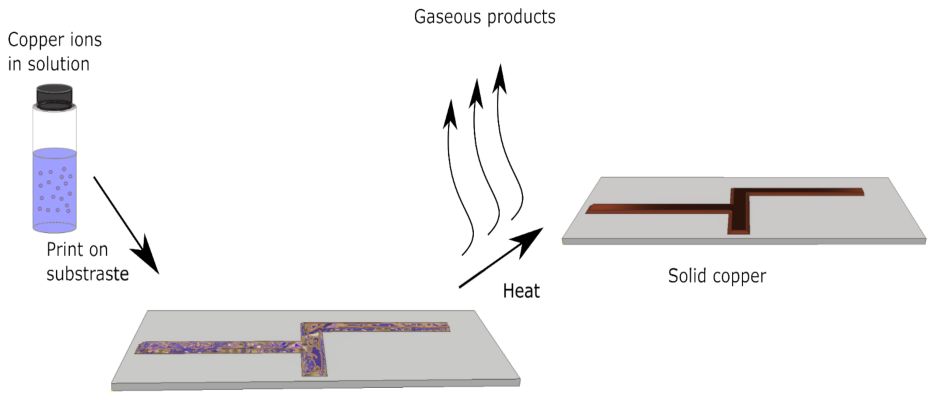

Figure 1.1: Schematic representation on how to produce a conductive layer with the use of Cu MOD ink. The MOD ink is printed on a substrate. Thermal treatment is then applied, whereupon the formate anions and amine ligands decompose and evaporate away, leaving a conductive Cu layer.

During the decomposition of the MOD ink something interesting happens, i.e. the Cu(II) complex decomposes to an intermediate Cu(I) complex before eventually reducing to metallic Cu(0)[3, 6]. Whats more, is that the decomposition temperature of the inks has been observed to vary depending on the Cu complex. In fact the salt $Cu[HCOO]_2$ shows an in situ reduction temperature up to 100°C higher compared to Cu amine complexes. Few studies have been devoted to understanding what contributes to this shift[6, 7, 8]. However, the recent study by Marchal et al. [3] has through direct investigation of the reduction pathway been able to relate the reduction temperature to two important factors. A reduced reduction temperature can be observed when the Cu(II) complexes transform to a Cu(I) intermediate with a strong structural resemblance, and whereupon the Cu(I) intermediates have a favorable stability. The stability of the Cu(I) intermediates are determined by the coordination geometry.

1.1 Objective and outline of thesis work

The aim of this study has been to investigate the Cu(II) and Cu(I) molecular structures from first principles methods. As Marchal et al. found that the reduction temperature is closely related to both the stability of the Cu intermediate and the structure resemblance to the Cu(II) state, the physics involved in the deduction of favorable MOD inks (with regards to lowest reduction temperature) are therefor based on quantum mechanics. With that in

mind, the theoretical tools used in this study are based on density functional theory (DFT) calculations, which have become a well established method in condensed matter physics and chemistry when dealing with N-electron quantum systems [9]. The Cu complexes considered in this study are the neat anhydrous Cu salt $Cu[HCOO]_2$ and the Cu complexes $Cu(Pyridine)_2[HCOO]_2$ and $Cu(Ethylenediamine)_2[HCOO]_2$. The DFT simulations will be performed on these molecular complexes in the gas phase and as crystal structures. In addition, vibrational analysis and molecular dynamics (MD) simmulations will be carried out to get some more insights to the dynamical properties as a function of temperature.

To begin with, Chapter 2 introduces some basic chemistry and theoretical background on crystalline materials in order to describe the properties of the MOD inks under consideration. Introduction to elementary quantum mechanics and the underlying theory behind the simulations are presented in Chapter 3. While Chapter 4 contains a more detailed review on how the theory is implemented in the applied software program, as well as other computational methods being used. Results and discussion following the calculations can be found in Chapter 5, and the conclusion of the work in Chapter 6. Meanwhile, suggestions for future work is presented in Chapter 7.

Chapter 2

Basics

The goal of this chapter is to introduce some basic chemistry to get more familiar with the Cu inks.

2.1 Chemistry

The theory presented in this section is based on the chemistry textbook [10].

2.1.1 Chemical Bonds

Chemical bonds are the attractive forces holding atoms together in a chemical compound. The attractive forces stem from various behaviours of the outermost electrons forming the chemical compound. The possible behaviours of the electrons are differentiated in different types of bonds.

When the outermost electron(s) are transferred between atoms, it will generate oppositely charged ions. The resulting electrostatic attraction between these ions are then said to form an ionic bond. This occurs typically between atoms with a large difference in their *electronegativity*, i.e. the tendency of an atom to attract shared electrons to itself. Whereas atoms with small electrongativities have to settle with sharing of one or more electron pairs, in order to obtain a stable electron configuration. This is known as *covalent bonding*, and is the most common bond found in nature [11]. For instance in hydrogen gas H_2, the hydrogen share an electron pair equally and are bonded covalently. The bond results from the mutual attraction for the shared electrons, due to the preferable noble gas electron configuration. Moreover, it is often ambiguous to differentiate between ionic and covalent bonds. therefore, bonds displaying both covalent and ionic character are called polar covalent bonds.

The collective term for bonding within a molecule is intramolecular bonding. Forces that causes the molecules to *aggregate*, to form a liquid or solid, are termed *intermolecular forces*. These forces can stem from ionic or covalent bonding, or they may arise from weaker interactions, e.g. dipole-dipole interaction and London dispersion interaction. For

instance in H_2O the intramolecular bonding is a polar covalent bond between the oxygen and hydrogen atoms. The oxygen attracts the electrons more than the hydrogen and becomes fractional negatively charged. It can therefore be seen as a electrical dipole, and two such molecules may then electrostatically attract each other. Now, having a container of several of water molecules, they will arrange themselves to have the best compromise between repulsion and attraction, and thus liquid water is formed. The attraction between the molecule dipoles are called dipole-dipole attraction.

At certain conditions noble gases are found in liquid and solid states, implying that there exists also a weak interaction between the noble atoms. Although the noble gases have no permanent electrical dipole moment, one has to take into account the intrinsic fluctuations at quantum level, i.e. the zero-point fluctuations in the charge distribution [12]. This results in fluctuating dipole moments, which can then induce a similar dipole moment at neighboring atoms, resulting to a force between them. This force that can occur between nonpolar molecules and noble gas atoms are called London dispersion forces.

For a solid system of metal atoms, the attractive force holding the atoms together arise from electrostatic forces between the conduction electrons. This form of bonding is called a metallic bonding. The bonding can be envisioned by imagining the valence electrons becoming dislocated form the nuclei, forming a sea of electrons which is sheared between the positively charged nuclei.

2.1.2 Coordination compounds

A coordination compound is a molecule consisting of a metal center with attached ligands. Ligands are either neutral or charged molecules that have a lone electron pair that can be utilized to form a bond to the metal. Typically in coordination compound the metal center is a complex ion, i.e. a transition metal ion, with additional counter ion(s) to balance the charge. The number of bonds formed between the ligands and a metal ion is called the *coordination number* and the ability of the complex ion to form ionic bonds is referred to as the *oxidation state*. Equivalently the oxidation state is the charge of the metal ion if the bonding were 100% ionic, i.e. no covalent component. This is a hypothetical charge, as no atoms are completely ionic. For instance the coordination complex $Cu(C_5H_5N)_2[HCOO]_2$ has an oxidation state of +2. This is denoted with roman numerals, i.e. Cu(II). Furthermore the pyridine (pyr) ligand C_5H_5N, is called a monodentate ligand, because it can only form one bond to a metal center. Whereas ethylenediamine (en) $C_2H_4(NH_2)_2$ can form two bonds and is therefore said to be a bidentate ligand. In the Figure 2.1 the coordination complex $Cu(en)_2[HCOO]_2$ is depicted. Here one can notice each (en) has two nitrogen which is bonded to the Cu ion. In addition it has a coordination number of 6, in a tetragonal distorted octahedral geometry. Moreover, Cu(II) complexes have a tendency to be in a 6 coordinated tetragonal distorted octahedral or a 5 coordinated square pyramidal or trigonal bipyramidal structure [13]. The Cu(I) complex tends to be in a 4 coordinated tetrahedral structure.

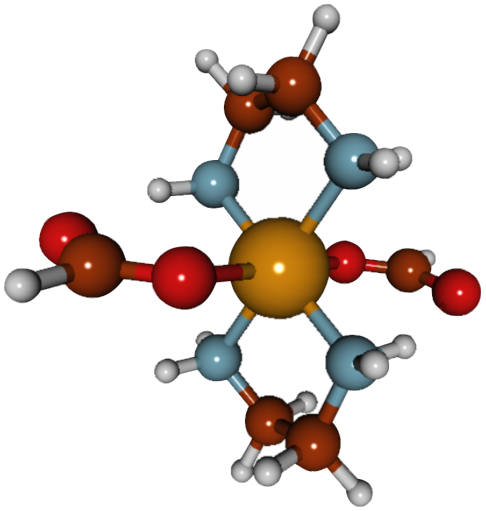

Figure 2.1: The color scheme denotes different type of atoms; orange(Cu), blue(nitrogen), white(hydrogen), red(oxygen) and brown(copper). The copper complex presented here is the $Cu(en)_2[HCOO]_2$ molecule.

2.2 Metallic organic decomposition inks

As earlier mentioned Marchal et. al. has investigated the decomposition of Cu(II) complex to metallic Cu(0) [3]. They were able to prove the existence of a Cu(I) intermediate for several Cu amine MOD inks. The reduction pathway for the MOD inks Cu(II) $\rightarrow$ Cu(I) is shown in Figure 2.2. However, the Cu(I) intermediate for anhydrous $Cu[HCOO]_2$ and $Cu(en)_2[HCOO]_2$ are assumed structures based on indirect measurements, while for the intermediate $Cu(I)_2(pyr)[HCOO]_2$ they were able to determine the structure from Extended X-Ray Absorption Fine Structure (EXAFS) measurements. They measured the reduction temperature for $Cu[HCOO]_2$, $Cu(en)_2[HCOO]_2$ and $Cu[HCOO]_2$ to 219 °C, 176 °C and 128°C respectively.

2.3 Crystalline solid

The periodically arrangement of groups of atoms constitutes what is called a crystal. Each group are equally spaced and the mathematical points at which they are attached to is called a lattice [14]. In three dimension the the lattice may be defined by three lattice translations vectors $\mathbf{a}_1$, $\mathbf{a}_2$ and $\mathbf{a}_3$ such that the crystal at position $\mathbf{r}$ looks identical from a point $\mathbf{r}$',

$$\mathbf{r}' = \mathbf{r} + u_1\mathbf{a}_1 + u_2\mathbf{a}_2 + u_3\mathbf{a}_3. \tag{2.1}$$

Where u_1, u_2 and u_3 are integers, and the set of points $\mathbf{r}$' that results from this equation defines the lattice. Depending on the crystal structure, suitable lattice translations vectors

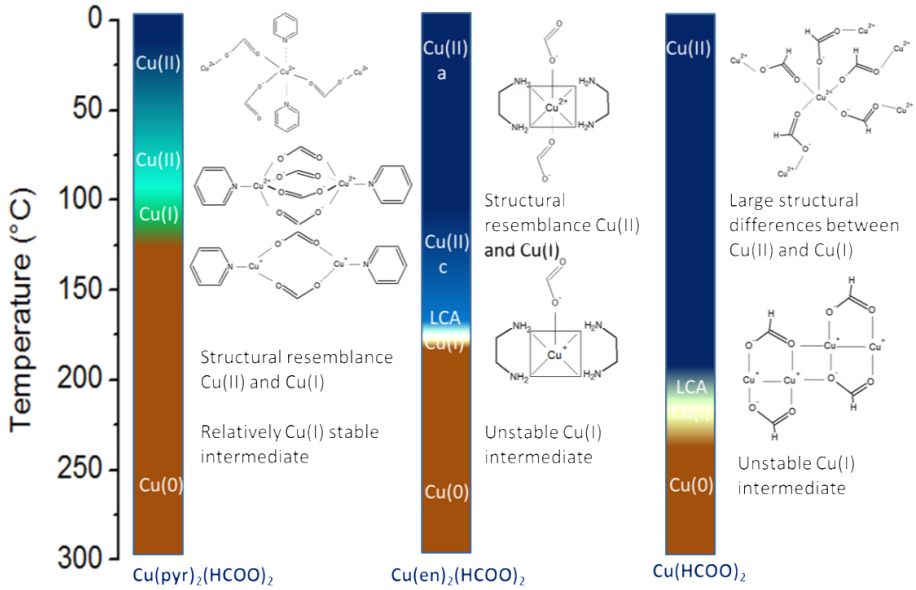

Figure 2.2: The reduction pathway for different MOD inks. The inks show different colors during the reduction process, shown by the color bar. The Figure is taken from the recent study [3].

are chosen which defines the *crystal axes*. Moreover, the lattice vectors span what is known as a unit cell. If the unit cell contains only a single atom and is constructed from a set of lattice vectors giving the minimum volume possible, the unit cell is said to be primitive.

Chapter 3

Quantum Mechanics

This chapter will first present some elementary quantum mechanics before describing briefly the underlying *Density functional theory*. The description is mainly based upon two books [15, 16]. Throughout this chapter, atomic units will be used.

3.1 Schrödinger Equation

Classical mechanics is insufficient for describing atoms and molecules at a fundamental level, where the electronic structure plays a crucial role in determining respective properties. In Erwin Schrödinger's wave function formulation the governing equation for electrons, atoms and molecules is the Schrödinger equation,

$$i\frac{\partial \Psi}{\partial t} = \hat{H}\Psi, \tag{3.1}$$

where Ψ is the wave function, describing completely the state of the system and $\hat{H}$ the Hamiltonian operator. For a system without time-dependent interactions one may use the time-independent Schrödinger equation,

$$\hat{H}\Psi = E\Psi, \tag{3.2}$$

where $\hat{H}$ operates on the wave function and one yields the eigenvalue, E, i.e. the energy of the system.

3.1.1 Many-electron Hamiltonian

Before embarking on how to solve the Schrödinger equation for atoms, molecules or solids the Hamiltonian needs to be defined. It is convenient to divide the total Hamiltonian

$$H_{\mathrm{tot}} = \hat{H}_{\mathrm{e}} + \hat{T}_{\mathrm{n}} + \hat{V}_{\mathrm{nn}}, \tag{3.3}$$

into an electronic Hamilton operator $\hat{H}_{\mathrm{e}}$, a kinetic energy operator $\hat{T}_{\mathrm{n}}$ for the nuclei and the nucleus-nucleus interaction energy operator $\hat{V}_{\mathrm{nn}}$. The electronic Hamilton operator for an isolated atomic or molecular system without any time-dependent interactions is,

$$\hat{H}_e = -\sum_{i=1}^{N_e} \frac{1}{2}\boldsymbol{\nabla}_i^2 - \sum_{i=1}^{N_e}\sum_{\alpha=1}^{N_n} \frac{Z_\alpha}{|\boldsymbol{R}_\alpha - \boldsymbol{r}_i|} + \sum_{i=1}^{N_e}\sum_{j>i}^{N_e} \frac{1}{|\boldsymbol{r}_i - \boldsymbol{r}_j|}. \tag{3.4}$$

Here Z_α denotes the charge of nucleus α, $\boldsymbol{R}_\alpha$ the position of the nucleus, $\boldsymbol{r}_i$ the position of the electron i and the number of particles constituting the system is N_e electrons and N_n nuclei. The electronic Hamiltonian can be written in a more compact form,

$$\hat{H}_e = \hat{T} + \hat{V}_{ne} + \hat{V}_{ee}, \tag{3.5}$$

where each of the three operators correspond to each term in equation (3.4) respectively, such that $\hat{T}$ is the kinetic energy operator, $\hat{V}_{\mathrm{ne}}$ is the energy operator due to attraction between the nucleus and electrons and $\hat{V}_{\mathrm{ee}}$ is the electron-electron energy repulsion operator. Further, the nucleus-nucleus repulsion energy operator is

$$\hat{V}_{nn} = \sum_{\alpha=1}^{N_n}\sum_{\beta>\alpha}^{N_n} \frac{Z_\alpha Z_\beta}{|\boldsymbol{R}_\beta - \boldsymbol{R}_\alpha|}, \tag{3.6}$$

and lastly, the kinetic energy operator for the nuclei, is defined as,

$$\hat{T}_n = \sum_{i=1}^{N_n} \frac{1}{2M_i}\boldsymbol{\nabla}_i^2, \tag{3.7}$$

where M_i is the mass of nucleus i.

3.1.2 Born-Oppenheimer approximation

There is a large mass difference between the electrons and nuclei which indicates that the velocities of the nuclei are much slower than for the electrons, such that the electrons arrange themselves as if the nuclei are at fixed positions. Thus the total wavefunction for the system can be decoupled into an electronic and nuclear wavefunction, since the electronic wave function only depends on the position of the nuclei, not their momentum, and the nuclei moves upon the resulting potential energy surface (PES) from the electronic wave function. That is,

$$\begin{aligned} \hat{H}_{\mathrm{tot}}\Psi_{\mathrm{tot}}(\boldsymbol{R},\boldsymbol{r}) &= E_{\mathrm{tot}}\Psi_{\mathrm{tot}}(\boldsymbol{R},\boldsymbol{r}) \\ \hat{H}_{\mathrm{e}}\Psi_{\mathrm{e}}(\boldsymbol{R},\boldsymbol{r}) &= E_e(\boldsymbol{R})\Psi_{\mathrm{e}}(\boldsymbol{R},\boldsymbol{r}) \\ (\hat{T}_{\mathrm{n}} + V_{\mathrm{nn}}(\boldsymbol{R}) + E_{\mathrm{e}}(\boldsymbol{R}))\Psi_{\mathrm{n}}(\boldsymbol{R}) &= E_{\mathrm{tot}}\Psi_{\mathrm{n}}(\boldsymbol{R}), \end{aligned} \tag{3.8}$$

where $\boldsymbol{R}$ is the nuclei coordinates, $\boldsymbol{r}$ the electronic coordinates and the subscript n denotes contributions from the nuclei. This is known as the Born-Oppenheimer approximation,

and a more rigorous derivation of the approximation can be found in [15]. Using the fact that in the electronic point of view, the nuclei are fixed objects exerting an external potential and the electron-nuclei attraction energy operator can then be rewritten,

$$\hat{V}_{\mathrm{ne}} = \sum_{i=1}^{N_e} \Big(\sum_{\alpha=1}^{N_n} \frac{-Z_\alpha}{|\boldsymbol{R}_\alpha - \boldsymbol{r}_i|} \Big) = \sum_{i=1}^{N_e} V_{\mathrm{ext}}(\boldsymbol{r}_i), \tag{3.9}$$

and for a fixed nuclei the nucleus-nucleus energy is simply,

$$V_{nn} = \langle \Psi_{\mathrm{e}} | \, \hat{V}_{\mathrm{nn}} \, | \Psi_e \rangle = \sum_{\alpha=1}^{N_n} \sum_{\beta<\alpha}^{N_n} \frac{Z_\alpha Z_\beta}{|\boldsymbol{R}_\beta - \boldsymbol{R}_\alpha|}. \tag{3.10}$$

3.1.3 Variational method

Normally it is not possible to obtain an analytic solution to the Schrödinger equation, even under the Born-Oppenheimer approximation. The *variational method* may then be used to find a upper bound for the ground state energy. For a given trial wavefunction, f, the expectation value of the Hamiltonian is larger or equal to the ground state energy. When the trial wave function yields the exact ground state energy E, then the trial wave function is the exact wave function [17]:

$$E \leq \frac{\langle f | \, \hat{H} \, | f \rangle}{\langle f | f \rangle} \tag{3.11}$$

3.2 Hartree-Fock

With regards to atoms and molecules, the Schrödinger equation has indeed only been solved exactly for the hydrogen atom. The electronic wave function for N electrons is a function of 4N variables, one spin and three spatial coordinates for each electron,

$$\Psi_{\mathrm{e}} = \Psi_{\mathrm{e}}(\boldsymbol{x}_1, \boldsymbol{x}_2, ...\boldsymbol{x}_N), \tag{3.12}$$

and thereby solving the Schrödinger equation quickly becomes tedious and impossible, even for many approximate methods. An important method within the electronic structure theory is the Hartree-Fock method. This method reduces the complexity by approximating the interactions between particles in an average manner.
The Hatree-Fock method starts out with the ansatz that the N-electron wave function is approximated by a product of N orthonormal spin orbitals $\psi_i(\boldsymbol{x})$, the *Slater determinant*[16],

$$\Psi_{\mathrm{HF}} = \frac{1}{\sqrt{N}} \begin{vmatrix} \psi_1(\boldsymbol{x}_1) & \psi_2(\boldsymbol{x}_1) & \cdots & \psi_N(\boldsymbol{x}_1) \\ \psi_1(\boldsymbol{x}_2) & \psi_2(\boldsymbol{x}_2) & \cdots & \psi_N(\boldsymbol{x}_2) \\ \vdots & \vdots & \ddots & \vdots \\ \psi_1(\boldsymbol{x}_N) & \psi_2(\boldsymbol{x}_N) & \cdots & \psi_N(\boldsymbol{x}_N) \end{vmatrix} \tag{3.13}$$

The prefactor of the determinant ensures the wave function is normalized. The spin orbital $\psi(\boldsymbol{x})$ is again a product of a spatial orbital $\phi_j(\boldsymbol{r})$ and a spin function $\sigma(s)$, hence the

coordinate $\boldsymbol{x} = (\boldsymbol{r}, \sigma)$ incorporates both the spatial coordinates and the spin. The spin orbital is a single-electron wavefunction which describes an electron with possible spin state, α-spin or β-spin. Furthermore, one knows from the Pauli principle that the wave function for a N-electron system must be anti-symmetric with respect to the exchange of two electrons. The product of spin orbitals as given in equation (3.13) satisfies such a requirement, i.e. the wave function changes sign when two particles are exchanged and one can also observe that two particles with the same spin cannot occupy the same spin orbital. This ensures that the exchange between the electrons will also be modelled when solving the Schrödinger equation. Moreover, the Born-Oppenheimer approximation is assumed and the expectation value of $\hat{H}_e$ is given by [15],

$$E_{\mathrm{HF}} = \langle \Psi_{\mathrm{HF}} | \, \hat{H} \, | \Psi_{\mathrm{HF}} \rangle = \sum_{i=1}^{N} H_i + \frac{1}{2} \sum_{i,j=1}^{N} (J_{ij} - K_{\mathrm{ij}}), \tag{3.14}$$

where

$$H_i = \int \psi_i^*(\boldsymbol{x}) \big[-\tfrac{1}{2} \boldsymbol{\nabla}^2 + v_{\mathrm{ext}}(\boldsymbol{x}) \big] d\boldsymbol{x}, \tag{3.15}$$

is the sum of the kinetic energy of an electron and the potential energy due the nuclear attraction. Furthermore,

$$J_{ij} = \int \int |\psi_i(\boldsymbol{x_1})|^2 \frac{1}{|\boldsymbol{r_1} - \boldsymbol{r_2}|} \big|\psi_j(\boldsymbol{x_2})^2\big| d\boldsymbol{x_1} \boldsymbol{x_2} \tag{3.16}$$

are called the *Coulomb integrals*, and represent the classical Coulomb interaction between the two charge clouds $|\psi_i(\boldsymbol{x_1})|^2$ and $|\psi_j(\boldsymbol{x_1})|^2$. Thus, a single electron interacts with the other electrons at their average position and not the instantaneous one. The last term in (3.14) has no classical counterpart, the *exchange integrals*,

$$K_{ij} = \int \int \psi_i^*(\boldsymbol{x_1}) \psi_j(\boldsymbol{x_1}) \frac{1}{|\boldsymbol{r_1} - \boldsymbol{r_2}|} \psi_i^*(\boldsymbol{x_2}) \psi_j(\boldsymbol{x_2}) d\boldsymbol{x_1} \boldsymbol{x_2}, \tag{3.17}$$

and originates from the anti-symmetric wavefunction with respect to exchange of two electrons. One knows from the variational principle, that the wave function giving the best approximation of the ground state, is the one with the smallest expectation value of energy. Now, minimizing the expectation value, $\langle \Psi_{\mathrm{HF}} | \, \hat{H} \, | \Psi_{\mathrm{HF}} \rangle$, subjected to the constraint that the spin orbitals are orthonormal,

$$\frac{\partial}{\partial \psi} \Big[\langle \Psi_{\mathrm{HF}} | \, \hat{H} \, | \Psi_{\mathrm{HF}} \rangle - \sum_{ij}^{N} \epsilon_{ij} (\langle \psi_i | \psi_j \rangle - \delta_{ij}) \Big], \tag{3.18}$$

with the Lagrangian multiplier, ϵ_{ij}, leads to a set of single electron equations, the *Hatree-Fock equations*,

$$\Big[-\tfrac{1}{2} \nabla^2 + V_{\mathrm{ext}}(\boldsymbol{x}) + V_H(\boldsymbol{x}) + V_X(\boldsymbol{x}) \Big] \psi_i(\boldsymbol{x}) = \sum_{j=1}^{N} \epsilon_{ij} \psi_j(\boldsymbol{x}), \tag{3.19}$$

where

$$V_H(\boldsymbol{x}) = \sum_{k=1}^{N} \int \frac{|\psi_k(\boldsymbol{x'})|^2}{|\boldsymbol{r} - \boldsymbol{r'}|} d\boldsymbol{x'} \tag{3.20}$$

is the Hatree potential and V_X describes the exchange potential,

$$V_X(\boldsymbol{x})\psi_j(\boldsymbol{x}) = \sum_{k=1}^{N} \int \psi_k^*(\boldsymbol{x'})\psi_j(\boldsymbol{x'}) \frac{1}{|\boldsymbol{r} - \boldsymbol{r'}|} \psi_k(\boldsymbol{x}) d\boldsymbol{x'}. \tag{3.21}$$

As can be seen from the Hatree-Fock equations, the spin orbitals ψ that solve the equations appear also in the exchange and the Hatree potential. Consequently, the solution must be found iteratively, i.e. Hartee-Fock method is a *self consistent field (SCF) method*.

In the Hatree-Fock theory there has been no restrictions regarding the spatial parts of α spin versus β spin, both the spatial parts and the number of α and β spins are allowed to differ. This scheme is called *unrestricted open-shell Hatree-Fock* (UHF) and enables for spin polarization. On the other hand, if the system is based on a *closed shell* configuration with even number of electrons, i.e. each spatial orbital ϕ_k is doubly occupied with a α and β spin and the rest of spin orbitals are empty, the Hatree-Fock equations simplify and the resulting scheme is called *restricted closed shell Hartree Fock-method* (RHF). An illustration of the different methods is shown if Figure 3.1. In the RHF case the 1s electrons are forced to have the same spatial description, while in the UHF method the two different 1s electrons experience different effective potentials (exchange interaction between the α-electrons), and thus prefer different spatial functions.

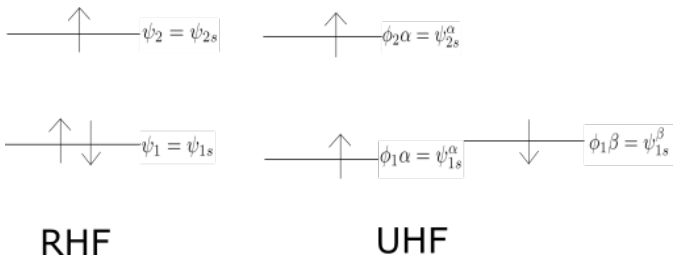

Figure 3.1: Electrons with two up spins, and one down spins are shown in the cases of RHF and UHF.

3.3 Density functional theory

The *Density functional theory* (DFT) represents an alternative to the Hatree-Fock approximation, by replacing the complex N-electron wave function and its associated Schrödinger equation with the electron density $\rho(\boldsymbol{r})$ and a new set of equations. The electron density

is defined as the integral over all but one of the spatial coordinates and all the spin coordinates,

$$\rho(\boldsymbol{r}) = N \int \cdots \int |\Psi(\boldsymbol{x}_1, \boldsymbol{x}_2, ..., \boldsymbol{x}_N|^2 ds \; d\boldsymbol{x}_2 \cdots d\boldsymbol{x}_n \tag{3.22}$$

and determines the probability of finding any of the N electrons within a volume element d$\boldsymbol{r}$. Integrating $\rho(\boldsymbol{r})$ gives then the total number of electrons,

$$\int \rho(\boldsymbol{r}) \; d\boldsymbol{r} = N. \tag{3.23}$$

Immediately one can start to understand why this would be beneficial compared to a wave function approach. Instead of having 4N variables describing the system, it is enough with three spatial coordinates, thus the dimensions are independent of the system size. In addition the following arguments from E.B Wilson helps to understand intuitively why the system is defined by the electron density[18],

- *The number of electrons in the system is defined from the integral of the density.*
- *The density is cusped at all nuclei, and only at the nuclei, and thus defines the position of the nuclei.*
- *The different types of nuclei are distinguished by the shape of the cusp.*

These comments were made under a conference in 1965, where Walter Kohn presented his seminal paper on DFT [19]. The foundations for DFT, e.g. the electron density uniquely determines all the properties of the system, rests upon the two theorems proved in Kohn's paper.

3.3.1 The Hohenberg-Kohn theorems

Recall that for an electronic system, the Hamiltonian is described by (3.4), and with the variational principle (3.11) the ground state energy and the ground state wavefunction can be determined. The Hohenberg-Kohn theorems demonstrates that the Hamiltonian operator is uniquely determined by the electron density and provides an analogous variational principle to that in the wave function approach with the electron density as a parameter[19].

Theorem 1: *The external potential $v_{\text{ext}}(\boldsymbol{r})$ and hence the Hamiltonian $\hat{H}$ are determined to within an additive constant by the electron density.*

Proof: Assume that another external potential, $v'_{\text{ext}}(\boldsymbol{r})$, is determined from the same electron density $\rho(\boldsymbol{r})$. Furthermore, the two external potentials are made such that they differ with more than a constant and thereby have different ground state wave function and energy (E and E'),

$$E = \langle\Psi|\,\hat{H}\,|\Psi\rangle = \langle\Psi|\,\hat{T} + \hat{V}_{\text{ee}} + \hat{V}_{\text{ext}}\,|\Psi\rangle = \langle\Psi|\,\hat{V}_{\text{ee}} + \hat{T}\,|\Psi\rangle + \int v_{\text{ext}}(\boldsymbol{r})\rho(\boldsymbol{r})d\boldsymbol{r}$$

$$E' = \langle\Psi'|\,\hat{H}'\,|\Psi'\rangle = \langle\Psi'|\,\hat{T} + \hat{V}_{\text{ee}} + \hat{V}'_{\text{ext}}\,|\Psi'\rangle = \langle\Psi'|\,\hat{V}_{\text{ee}} + \hat{T}\,|\Psi'\rangle + \int v'_{\text{ext}}(\boldsymbol{r})\rho(\boldsymbol{r})d\boldsymbol{r}.$$

An assumption is also made that the ground state is non-degenerate. With Ψ' as a trial function for the ground state energy E, the variational principle (3.11) becomes,

$$\begin{aligned} E < \langle\Psi'|\,\hat{H}\,|\Psi'\rangle &= \langle\Psi'|\,\hat{V}_{\text{ee}} + \hat{T}\,|\Psi'\rangle + \int v_{\text{ext}}(\boldsymbol{r})\rho(\boldsymbol{r})d\boldsymbol{r} \\ &= E' - \int \big(v_{\text{ext}}(\boldsymbol{r}) - v'_{\text{ext}}(\boldsymbol{r})\big)\rho(\boldsymbol{r})d\boldsymbol{r} \end{aligned} \tag{3.24}$$

If one then repeats the same procedure with Ψ as a trial function for the ground state energy E', then,

$$E' < E - \int \big(v'_{\text{ext}}(\boldsymbol{r}) - v_{\text{ext}}(\boldsymbol{r})\big)\rho(\boldsymbol{r})d\boldsymbol{r}. \tag{3.25}$$

Addition of (3.24) and (3.25) results in

$$E + E' < E + E', \tag{3.26}$$

which is a contradiction, and thus different external potentials will always result in different electron densities. (There is a one-to-one correspondence between the external potentials and the electron densities). Since the external potential is uniquely determined by the electron density, it follows that the Hamiltonian is also uniquely defined and hence also the ground state wave function and energy. One should then be able to write the ground state energy as a functional of density, i.e

$$\begin{aligned} E &= T[\rho] + V_{\text{ee}}[\rho] + \int v_{\text{ext}}(\boldsymbol{r})\rho(\boldsymbol{r})d\boldsymbol{r} \\ &= F[\rho] + \int v_{\text{ext}}(\boldsymbol{r})\rho(\boldsymbol{r})d\boldsymbol{r} = E[\rho] \end{aligned} \tag{3.27}$$

Here, the brackets denote that the electron density determines the ground state energy, i.e. that energy is a *functional* of electron density. Moreover, (3.27) defines $F[\rho]$ which is independent of the system at hand(the external potential) and is said to be a *universal functional*. If the universal functional was to be known, the Schrödinger equation would have been solved exactly. Unfortunately, the explicit form is unknown.

Theorem 2: *For a given trial density $\rho'(\boldsymbol{r})$, that fulfills $\rho'(\boldsymbol{r}) \geq 0$ and $\int \rho'(\boldsymbol{r})d\boldsymbol{r} = N$, the ground state energy E_0 is less or equal to $E_v[\rho']$,*

$$E_0 \leq E_v[\rho'], \tag{3.28}$$

and equality is achieved when the trial density is the true ground state density.

Proof: From previous discussion one knows that a trial density ρ' defines its own wave function Ψ'. The proof follows then readily from the variational method for wave functions (3.11), and normalized wavefunction is assumed for simplicity:

$$E_0[\rho] \leq \langle \Psi' | \hat{H} | \Psi' \rangle = E[\rho']. \tag{3.29}$$

Equality occurs when the trial density produces the exact ground state wave function and consequently the trial density is then the exact ground state density.

For simplicity the ground state was assumed non-degenerate in the preceding discussion. Degenerate ground states presents no difficulties, and the treatment has been done by Levi with the *constrained-search* formulation [20],

$$\begin{aligned} F[\rho] &= \langle \Psi | \hat{T} + \hat{V}_{\mathrm{ee}} | \Psi \rangle \\ &= \min_{\Psi \to \rho} \langle \Psi | \hat{T} + \hat{V}_{\mathrm{ee}} | \Psi \rangle . \end{aligned} \tag{3.30}$$

Here the search is over all the antisymmetric wave functions, giving the input density ρ, such that $F[\rho]$ delivers the minimum of $\langle \hat{T} + \hat{V}_{\mathrm{ee}} \rangle$.

3.3.2 The Kohn-Sham scheme

It is tantalizing that the ground state energy, equation (3.27), could be obtained from a stationary principle required by the variational method (3.28),

$$\delta \{ E[\rho] - \mu \int \rho(\boldsymbol{r}) d\boldsymbol{r} \} = 0, \tag{3.31}$$

where the ground state energy is minimized with respect to the electron density and μ is a Lagrangian multiplier associated with the constraint $\int \rho(\boldsymbol{r}) d\boldsymbol{r} = N$. Inserting the ground state energy (3.27), results in the Euler-Lagrange equation,

$$\mu = \frac{\delta E[\rho]}{\delta \rho(\boldsymbol{r})} = v_{\mathrm{ext}}(\boldsymbol{r}) + \frac{\delta F[\rho(\boldsymbol{r})]}{\delta \rho(\boldsymbol{r})}, \tag{3.32}$$

The Euler-Lagrange equation (3.32) gives multiple solutions, associated with extrema of $E[\rho]$, so the one which minimizes $E[\rho]$ must be chosen. This direct approach requires that the functional $F[\rho]$ is expressed as a functional of density, or optionally an approximate $F[\rho]$ is constructed [16]. The $F[\rho]$ functional contains the kinetic energy, and small inaccuracies describing this functional can lead to large errors. Kohn and Sham invented an approach where the kinetic energy functional is split into two terms, with one term that is calculated exactly while the other is a small correction part[21].

To treat a physical interacting system the Kohn-Sham method constructs a fictional non-interacting ground state Ψ_{KS}, giving rise to the same electron density $\rho(\boldsymbol{r})$ and chemical potential μ as the interacting ground state Ψ_0. The Hamiltonian for the interacting system is given by (3.4) and for the non-interacting case,

$$\hat{H}_s = \hat{T} + \sum_i^N v_{\mathrm{ext}}(\boldsymbol{r}_i), \tag{3.33}$$

with a corresponding determinantal wave function (3.13) as in the Hatree-Fock theory, where the N spin orbitals and here the Kohn-Sham (KS) orbitals ψ_i are solutions to the one-electron Schrödinger equation,

$$\hat{h}_{\mathrm{KS}}\psi_i = [-\tfrac{1}{2}\nabla^2 + v_{\mathrm{eff}}(\boldsymbol{r})]\psi_i = \epsilon_i\psi_i, \tag{3.34}$$

For the determinantal wave function the electron density (3.22) reduces to

$$\rho(\boldsymbol{r}) = \sum_i^N \sum_s |\psi_i(\boldsymbol{r}, s)|^2, \tag{3.35}$$

and the kinetic energy functional for the fictitious non-interacting electrons is given by

$$T_s[\rho] = \min_{\Psi\to\rho} \langle\Psi|\,\hat{T}\,|\Psi\rangle = \min_{\sum|\psi|^2=\rho} \big[\sum_i^N \langle\psi_i| - \tfrac{1}{2}\nabla^2\,|\psi_i\rangle\,\big], \tag{3.36}$$

where a constrained search is done over all single determinantal wave functions Ψ yielding the true density ρ. The quantity $T_s[\rho]$ differs from the true kinetic energy functional $T[\rho]$, defined in (3.27), and the residual term is absorbed into a *exchange and correlation functional* $E_{\mathrm{xc}}[\rho]$. The ground state energy for an interacting system is then,

$$E[\rho] = T_s[\rho] + J[\rho] + E_{\mathrm{xc}}[\rho] + \int \rho(\boldsymbol{r}) v_{\mathrm{ext}}(\boldsymbol{r}) d\boldsymbol{r}, \tag{3.37}$$

with $E_{\mathrm{xc}}[\rho]$ defined as,

$$E_{\mathrm{xc}} \equiv T[\rho] - T_s[\rho] + V_{\mathrm{ee}}[\rho] - J[\rho], \tag{3.38}$$

which contains also the difference between the classical and non-classical part of the electron-electron repulsion energy V_{ee}. The classical part is given by the Hartree electrostatic energy,

$$J[\rho] = \frac{1}{2}\int\int \frac{\rho(\boldsymbol{r}')\rho(\boldsymbol{r})}{|\boldsymbol{r}-\boldsymbol{r}'|} d\boldsymbol{r} d\boldsymbol{r}'. \tag{3.39}$$

The new ground state energy functional $E[\rho]$ inserted in the Euler-Lagrange equation (3.32) gives

$$\frac{\delta T_s}{\delta\rho(\boldsymbol{r})} + \frac{\delta J}{\delta\rho(\boldsymbol{r})} + \frac{\delta E_{\mathrm{xc}}}{\delta\rho(\boldsymbol{r})} + v_{\mathrm{ext}}(\boldsymbol{r}) = \mu, \tag{3.40}$$

and results in the same solution as the non-interacting Euler-Lagrange,

$$\frac{\delta T_s}{\delta\rho(\boldsymbol{r})} + v_{\mathrm{eff}}(\boldsymbol{r}) = \mu, \tag{3.41}$$

so that v_{eff} becomes

$$v_{\mathrm{eff}}(\boldsymbol{r}) = v_{\mathrm{ext}}(\boldsymbol{r}) + \int \frac{\rho(\boldsymbol{r}')}{|\boldsymbol{r}-\boldsymbol{r}'|} d\boldsymbol{r}' + v_{\mathrm{xc}}(\boldsymbol{r}), \tag{3.42}$$

where the exchange-correlation potential is defined as

$$v_{\mathrm{xc}}(\boldsymbol{r}) = \frac{\delta E_{\mathrm{xc}}[\rho]}{\delta \rho(\boldsymbol{r})}. \tag{3.43}$$

This is a key part of the Kohn-Sham scheme; from the functional dependence of (3.37), an effective potential can be extracted that is felt by the fictitious non-interacting electrons of the same density. Moreover, the effective potential depends on the density $\rho(\boldsymbol{r})$, hence it must be solved together with equations (3.34) and (3.35) self-consistently. The set of equations make up the *Kohn-Sham equations*, and when the wave function and density is found the total energy can be computed through (3.37). The Kohn-Sham equations can in principle be solved exactly, however the exchange-correlation functional is not known, and must be approximated.

One can also observe that the Kohn-Sham equations are on the same form as the Hatree-Fock equations, except that they contain a more general local potential $v_{\mathrm{eff}}(\boldsymbol{r})$. Owing to the fact that orbitals have been reintroduced to evaluate the non-interacting reference system, the complexity has been increased from 3 to 3N variables. In comparison to the Hatree-Fock method, the Kohn-Sham scheme incorporates fully (albeit approximated) the exchange and correlation effect of electrons, whereas the Hartree-Fock method lacks any electron-correlation contribution. There are extensions to the Hartree-Fock method, which incorporates the correlation effect of electrons, on the expense of added computational cost [15]. These methods go under the name *post-Hartree—Fock* methods.

3.3.3 Exchange correlation

The reaming part of establishing an approach to solve the ground state energy for a N-electron problem within the Kohn-Sham scheme, is to find the exchange-correlation potential (3.43). The exact form of the $E_{\mathrm{xc}}[\rho]$ is unknown and one thus needs to find an approximate expression for $E_{\mathrm{xc}}[\rho]$. There are some guidelines as to what properties such approximation should obey, based on the known properties of the exact functional [22]. Over the years many different approximate $E_{\mathrm{xc}}[\rho]$'s have been created and to categorize them Perdew suggested a "Jacob's ladder", in which the form of $E_{\mathrm{xc}}[\rho]$ defines the different rungs [22]. Going up the ladder increases complexity, but with an expected improvement in the accuracy.

Local Density Approximation

The simplest of the approximations is the *Local density approximation* (LDA), wherein the exchange-correlation functional depends only on the electron density. Also, the electron density is assumed to exhibit the same nature as a uniform electron gas. That is, the electron density is divided into infinitesimal volumes, such that the inhomogeneous nature vanishes and can be replaced by the density of a uniform electron gas. The LDA for the exchange-correlation energy is then [16],

$$E_{\mathrm{xc}}^{LDA}[\rho] = \int \rho(\boldsymbol{r}) \epsilon_{\mathrm{xc}}(\rho(\boldsymbol{r})) d\boldsymbol{r} \tag{3.44}$$

where $\epsilon_{\rm xc}(\rho)$ is the exchange and correlation energy per particle of a uniform electron gas. Accurate values of this parameter has been found from quantum Monte Carlo calculations [23], and thus the Kohn-Sham equations may be solved. One should note that the LDA is justified for systems with slowly varying electron densities, typically metallic systems. However, successful results have been obtained for highly inhomogeneous systems as well, which may be attributed to the fact that LDA functional satisfy many formal properties of the exact exchange-correlation functional, e.g. so called sum rules [24, 16, 25, 26].

Generalized Gradient Approximation

To improve upon the LDA approach, which only depends on the electron density, the *Generalized Gradient Approximation* (GGA) was invented. This method includes additional information about the derivatives of the electron density at a given point. Inclusion of the gradient of density in the exchange-correlation functional has been done in a several ways, but their general form is [27],

$$E_{\rm xc}^{GGA}[\rho] = \int f^{GGA}(\rho(\boldsymbol{r}), \nabla\rho(\boldsymbol{r}))d\boldsymbol{r} \tag{3.45}$$

where f^{GGA} is some function with the density and its gradient as parameters. The functional can be separated into two terms,

$$E_{\rm xc}^{GGA}[\rho] = E_{\rm x}^{GGA}[\rho] + E_{\rm c}^{GGA}[\rho] \tag{3.46}$$

containing the exchange and correlation contribution respectively. The exchange functional takes the form

$$E_{\rm x}^{GGA}[\rho] = \int \rho(\boldsymbol{r})\epsilon_{\rm x}^{unif}(\rho(\boldsymbol{r}))F_{\rm x}^{GGA}(s(\boldsymbol{r}))d\boldsymbol{r} \tag{3.47}$$

with ϵ_x^{unif} is identical to the exchange energy per particle in (3.44) when $\epsilon_{\rm xc}$ is separated in a similar fashion to (3.46). Furthermore, F_x^{GGA} is the exchange enhancement factor, telling how much exchange energy is enhanced over its LDA value, and is a function of [24],

$$s(\boldsymbol{r}) = \frac{|\nabla\rho(\boldsymbol{r})|}{2(3\pi^2)^{1/3}\rho(\boldsymbol{r})^{4/3}}, \tag{3.48}$$

a dimensionless parameter called the reduced density gradient. To give an idea what the enhancement factor might look like, two popular GGA exchange functional will be presented, the Perdew-Burke-Ernzerhof (PBE, [28]) and Becke88 (B88, [29]) functionals,

$$F_x^{\rm PBE}(s) = 1 + \kappa - \frac{\kappa}{1 + \mu s^2/\kappa} \tag{3.49}$$

$$F_x^{\rm B88}(s) = 1 + \frac{\beta x(s)^2}{[1 + 6\beta x(s)\sinh^{-1}(x(s))]}, \quad x(s) = (48\pi)^{1/3}s \tag{3.50}$$

For the PBE functional the parameters κ and μ are derived from physical constraints the exact functional should posses, i.e. PBE is a *non-emperical* functional. On the other hand, the unknown parameter β for B88 is obtained from fitting to exact atomic Hatree-Fock exchange data, i.e. B88 is an *emperical* functional. We can observe that in the limit of a uniform electron gas, $F_x(0) = 1$ and both functionals returns the LDA exchange.

The functional form of the GGA correlation functional E_c^{GGA} is also a complex function of a reduced gradient, and the function may come in different forms, e.g. the PBE correlation functional [28] and LYP [30]. Besides, the magnitude of the functional is generally <10% of the exchange energy, so it is more important that the exchange functional is accurate[31]. Hence for brevity's shake, the form of this functional will not be presented here.

Hybrid

The LDA and GGA approach were the first two rungs of "Jacob's ladder". The natural extension to the GGA method is then to include higher order derivatives of the electron density. The *meta-GGA*s use the Laplacian of the density $\nabla^2\rho$ and/or the orbital kinetic density $\tau(\boldsymbol{r}) = \frac{1}{2}\sum_i |\nabla\phi_i(\boldsymbol{r})|^2$ [15].

The next rung on the ladder is the *hybrid* functionals, which includes fractions of the exact Hatree-Fock exchange. The justification for this mixing stems from the adiabatic connection formula [32],

$$E_{\mathrm{xc}}[\rho] = \int_0^1 E_{\mathrm{xc},\lambda} d\lambda. \tag{3.51}$$

Here λ is a coupling parameter characterizing the strength of the electron-electron interaction, i.e switches on the Coulomb repulsion $1/|\boldsymbol{r}' - \boldsymbol{r}|$. $E_{\mathrm{xc},\lambda}$ is the potential energy of exchange and correlation at λ. The formula connects the fictitious non-interacting Kohn-Sham system ($\lambda = 0$) with the real system $\lambda = 1$, through a continuum of partially interacting real systems, all with the same electron density. In the limit of $\lambda = 0$ there is no correlation energy, only the Hatree-Fock exchange energy (with Kohn-Sham orbitals), thus it is possible to envisage why the Hartee-Fock exchange might contribute to a better exchange-correlation functional. LDA, GGA, and meta-GGAs have been mixed with fractions of Hatree-Fock exchange to construct new functionals. The PBE0 functional [33]

$$E_{\mathrm{xc}}^{PBE0} = \frac{1}{4}E_x^{HF} + \frac{3}{4}H_{\mathrm{x}}^{PBE} + E_c^{PBE} \tag{3.52}$$

mixes a fourth of Hatree-Fock exchange with three quarters of the PBE exchange along with with the full PBE correlation.

3.3.4 Unrestricted Kohn-Sham

Up to this point the theory on DFT has been restricted to systems with only scalar external potential and no separation of the α- and β-electron densities, $\rho^\alpha(\boldsymbol{r})$ and $\rho^\beta(\boldsymbol{r})$ respectively. The theory with $\rho^\alpha(\boldsymbol{r})$ and $\rho^\beta(\boldsymbol{r})$ as basic variables instead of the electron density

is called *spin-density-functional theory* or sometimes *Unrestricted Kohn-Sham* (UKS) approach. The derivation of this theory can be done in a similar fashion as for the restricted Kohn-Sham scheme. Further details are for instance found in [16, 34]. Here the existence of an universal functional is proved, i.e one-to-one correspondence between spin electron densities and spin dependent external potentials, $v_{\text{ext},\sigma}(\boldsymbol{r})$. Where σ is an electron with either α- or β-spin. The universal function is then,

$$F[\rho^\alpha, \rho^\beta] = T_s[\rho^\alpha, \rho^\beta] + J[\rho] + E_{\text{xc}}[\rho^\alpha, \rho^\beta] \tag{3.53}$$

where $\rho = \rho^\alpha + \rho^\beta$ is the total density and definition of J[ρ] is the same as in the restricted case. The Kohn-Sham equations are

$$\begin{aligned} \hat{h}^\sigma \phi_{i\sigma}(\boldsymbol{r}) &= [-\tfrac{1}{2}\boldsymbol{\nabla}^2 + v^\sigma_{\text{eff}}]\phi_{i\sigma}(\boldsymbol{r}) \\ &= \frac{\epsilon'_{i\sigma}}{n_{i\sigma}}\phi_{i\sigma} = \epsilon_{i\sigma}\phi_{i\sigma}(\boldsymbol{r}), \quad i = 1, 2, ..., N^\sigma, \end{aligned} \tag{3.54}$$

with the spin-dependent effective potentials

$$v^\sigma_{\text{eff}} = v_{\text{ext},\sigma}(\boldsymbol{r}) + \int \frac{\rho(\boldsymbol{r}')}{|\boldsymbol{r} - \boldsymbol{r}'|} d\boldsymbol{r}' + \frac{\delta E_{\text{xc}}[\rho^\alpha, \rho^\beta]}{\delta \rho^\alpha(\boldsymbol{r})} \tag{3.55}$$

where $\epsilon'_{i\sigma}$ are the Lagrangian multipliers associated with the normalization constraints and $n_{i\sigma}$ is the occupation numbers,

$$\rho^\sigma(\boldsymbol{r}) = \sum_i n_{i\sigma} |\phi_{i\sigma}(\boldsymbol{r})|^2. \tag{3.56}$$

In practice the lowest eigenstates are chosen to be occupied completely ($n_{i\sigma} = 1$) and the rest are unoccupied ($n_{i\sigma} = 0$). The number of electrons with σ-spin needs to be varied as well to achive minumum, subjected to the constraint

$$N = N^\alpha + N^\beta. \tag{3.57}$$

These equations constitute the self-consistent field method of UKS method. As discussed in the end of the Hatree-Fock section 3.2, this allows for spin polarization. Electrons of different spins may have different spatial densities, hence the effective potential in equation (3.55) may then be different. Resulting in a self-consistent solution where the total spin density $\rho^\alpha(\boldsymbol{r}) - \rho^\beta(\boldsymbol{r})$ is different from zero, and thus this theory can describe spontaneous magnetization. In addition, this theory allows for an external magnetic field acting on the spins of the electrons.

The exchange-correlation functional $E[\rho^\alpha, \rho^\beta]$ is dependent on the spin-electron densities. For brevity the derivation of the different approximations will not be done here and the reference given in the respective subsections in section 3.3.3 should be consulted. However for completeness, the general form of the LDA and GGA will be presented.

$$E^{LSDA}_{\text{xc}}[\rho^\alpha, \rho^\beta] = \int \rho(\boldsymbol{r}) \epsilon_{\text{xc}}(\rho^\alpha(\boldsymbol{r}), \rho^\beta(\boldsymbol{r})) d\boldsymbol{r} \tag{3.58}$$

is the extended version of LDA, the *Local Spin Density Approximation* (LSDA) with ϵ_{xc} as the exchange-correlation energy per particle for an electron in an uniform electron gas with spin density ρ^{σ}. The general form of the GGA methods are

$$E_{\text{xc}}^{GGA}[\rho^{\alpha}, \rho^{\beta}] = \int f^{GGA}(\rho^{\alpha}(\boldsymbol{r}), \rho^{\beta}(\boldsymbol{r}), \nabla\rho^{\alpha}(\boldsymbol{r})\nabla\rho^{\beta}(\boldsymbol{r}))d\boldsymbol{r} \tag{3.59}$$

with f^{GGA} being a function with the different spin-electron density and gradients as parameters. The hybrid functionals for the unrestricted spin case is equivalent to the restricted case, with the exception that one uses the unrestricted LSDA/GGA functionals instead.

3.4 Basis set

To use the Hatree-Fock or the Kohn-Scham method as a computational method one would need to approximate the spin orbitals and the KS orbitals. These unknown orbitals are expanded in terms of a set of known functions χ, e.g plane waves, exponential, wavelets or Gaussian functions. If the expansion is done in a complete basis set, that is using infinitely number of functions to describe the orbital, the representation is exact. However, as this requires an infinite number of functions, one needs to use a finite basis set. Hence, decreasing the basis set size, results in a poorer representation of the orbital, but at less computational cost. The choice of a the basis function will also effect the accuracy and computational cost. In general a good basis function should mimic the behavior of the physical problem, so convergence of the basis set size occurs rather swiftly [15].

3.4.1 Gaussian type orbitals

A normal practice in quantum chemistry is to model the spin/KS orbitals with an atom centered basis set. Which typically include either Slater type orbital (STO) or Gaussian type orbitals (GTO). Computational methods in this work are based on GTO and for that reason no further elaboration on the STO basis set will be made. The GTO satisfy the guideline that the basis function should have behaviour agreeing with the physics of the problem. In the sense that GTO have the correct long range properties, i.e. decays to zero when moving radially far out. The GTO have the following form in polar coordinates,

$$\chi_{\zeta,n,l,m}(r,\theta,\phi) = NY_{l,m}(\theta,\phi)r^{2n-2-l}e^{-\zeta r^2}, \tag{3.60}$$

with $Y_{l,m}(\theta,\phi)$ as the spherical harmonics, where *l* and *m* are the orbital angular momentum- and the magnetic- quantum number respectively. N is a normalization constant, and the Gaussian function, often called a primitive Gaussian function, with its exponent, ζ, determining the width of the function. Large ζ gives a localized function, whereas a small value would give a diffuse function. Each spin/KS orbital can then be written as a linear combination of GTO,

$$\psi_i = \sum_{\alpha} c_{\alpha i}\chi_{\alpha} \tag{3.61}$$

where $c_{\alpha i}$ determines the weight of each basis function, and are determined during the self-consistent field method. For computational efficiency it is common to make a linear combination of several GTO into a new contracted GTO [**?**],

$$\begin{aligned}\psi_i &= Y_{l_i,m_i} \sum_\alpha c_{\alpha i} \sum_j d_{\alpha j} e^{-\zeta r^2} \\ &= \sum_\alpha c_{\alpha i} \varphi_\alpha(r)\end{aligned} \tag{3.62}$$

Here j sums through the length of the contraction, $c_{\alpha i}$ is the weight of each contracted GTO and $d_{\alpha j}$ is the contraction coefficient. The contraction coefficients and the exponent, i.e. the contraction basis function $\varphi(\boldsymbol{r})$, are determined prior to the calculation depending on desired qualities. This has the advantage that one can optimize several GTO at the same time. The smallest number of contracted basis functions one would need to contain all the electrons of a neutral atom is a *minimum basis set*, i.e. one contracted basis function for each atomic orbital in a closed shell (1s, 2s, p_x, p_y, p_z ...) This is in most cases inadequate, and improvement can be realized upon doubling of all the contracted basis functions, known as a *Double Zeta* type basis. Further improvements can be done by tripling the basis functions *Triple Zeta*, or increasing even further *Quadruple Zeta*, *Quintuple Zeta* and so on. Moreover, to achieve accurate results it is often necessary to include *polarization functions* as well [15]. Polarization functions are basis functions with angular momentum of higher order compared to the valence electrons. This allows for polarization of the valence orbitals such that the bond in a molecule is better described.

3.4.2 Plane Waves Basis Set

An alternative method to the GTO expansion is to expand the KS orbitals in *plane wave* basis functions. The method rely on the Bloch's theorem which states that an electron in a periodic system, like solids, can be represented by a *Bloch wave*[35],

$$\psi_{j,\boldsymbol{k}}(\boldsymbol{r}) = e^{i\boldsymbol{k}\cdot\boldsymbol{r}} u_{j,k}(\boldsymbol{r}), \tag{3.63}$$

which is a plane wave characterized with wave vector $\boldsymbol{k}$ times a function $\mathrm{u}_{\boldsymbol{k}}(\boldsymbol{r})$ with the same periodicity as the lattice, i.e. $\mathrm{u}_{\boldsymbol{k}}(\boldsymbol{r}+\boldsymbol{R}) = \mathrm{u}_{\boldsymbol{k}}(\boldsymbol{r})$ with R being the Bravais lattice vector. Consequently for a crystalline solid, the one-electron Schrödinger-like equation models an electron in an effective periodic potential, such that the Bloch's theorem can be utilized by expanding the KS orbitals in Bloch waves $\psi_{i,\boldsymbol{k}}$. The periodic potential $u_{\boldsymbol{k}}$ can be Fourier expanded in terms of the reciprocal lattice vector $\boldsymbol{G}$ which results in

$$\psi_{j,\boldsymbol{k}} = \sum_{\boldsymbol{G}} C_j(\boldsymbol{k},\boldsymbol{G}) e^{i(\boldsymbol{k}+\boldsymbol{G})\cdot\boldsymbol{r}}, \tag{3.64}$$

where $\mathrm{C}_j(\boldsymbol{k}+\boldsymbol{G})$ is a Fourier expansion coefficient and the summation is over all values of $\boldsymbol{G}$. One therefore needs an infinite number of plane waves to represent the KS orbital. In practice only plane waves with wave vectors within a sphere of radius $\boldsymbol{G}$ is chosen. On the basis that the effective KS potential (3.42) converges rapidly with increasing G [36], plane waves with kinetic energy higher than some energy cutoff E_{cut} is truncated,

$$\frac{1}{2}|\boldsymbol{k}+\boldsymbol{G}| \leq E_{\mathrm{cut}}, \tag{3.65}$$

then the basis functions become,

$$\psi_{j,\boldsymbol{k}} = \sum_{|\boldsymbol{G}+\boldsymbol{k}|\leq G_{\text{cut}}} C_j(\boldsymbol{k},\boldsymbol{G}) e^{i(\boldsymbol{k}+\boldsymbol{G})\cdot\boldsymbol{r}}. \tag{3.66}$$

The plane wave basis set then consists of basis wave functions (3.66) solving the one electron Schrödinger equation (3.34) with eigenvalues $\epsilon_j(\boldsymbol{k})$. The eigenvalues constitute the band structure of the crystal where $j = 1, 2, ..$ is a discrete set and the wave vector $\boldsymbol{k}$ is any value in the primitive cell in k-space, *the first Brillouin zone* (BZ)[37]. The electron density for a periodically repeated unit cell with volume Ω is then,

$$\begin{aligned}\rho(\boldsymbol{r}) &= \frac{1}{\Omega}\sum_j \int_{\text{BZ}} f_j(\boldsymbol{k}) \sum_{\boldsymbol{G}\boldsymbol{G}'} c_j^*(\boldsymbol{k},\boldsymbol{G}') c_j(\boldsymbol{G},\boldsymbol{k}) e^{i(\boldsymbol{k}+\boldsymbol{G})\cdot r} d\boldsymbol{k} \\ &= \sum_{\boldsymbol{G}} \rho(\boldsymbol{G}) e^{i\boldsymbol{G}\cdot r},\end{aligned} \tag{3.67}$$

with $\mathrm{f}_j(\boldsymbol{k})$ as the occupation number associated with state j. For practical calculations the integral must be approximated by a finite sum over a set of $\boldsymbol{k}$-points. The number of $\boldsymbol{k}$-points required for accurate results depends on the dispersion of occupied bands and hence, the system under study [38].

3.4.3 Pseudopotentials

The physical interesting properties are to a large degree determined by the valence electrons, such as excitations, conductivity, bond breaking and bound formation. Meanwhile, the description of the strongly localized core electrons at the nuclei require numerous rapidly oscillating functions, i.e plane wave basis with a high energy cutoff [39]. Treating the core electrons comes then at a high computational cost even though they are less important. A procedure to deal with this is to use *pseudopotentials*. The Coulomb potential of the nucleus and the core electrons are replaced by an effective nuclear potential screened by the core electrons. The pseudopotential is an angular momentum-dependent potential such that all the interactions between the valence electrons and the core are accounted for. These are; Pauli repulsion, exchange and correlation effects with the core electrons and the effective nuclear Coulomb attraction**??**. Outside the core region this potential should reproduce the true potential and result in the true wave function. Inside the core the potential is a weaker potential than the true potential and the "pseudized" wave functions become much smoother and ideally with no nodal structure. This approximation allows for smaller energy cutoff, hence smaller basis sets. In addition, relativistic effects can be partly accounted for, by incorporating them in the pseudopotentials.

Chapter 4

Computational methods

The computational methods used in this thesis has been carried out using the open source software package CP2k[40]. CP2K is a quantum chemical and solid states physics package convenient for several different modeling methods, e.g. a framework for DFT calculations, but also Molecular dynamics, Molecular mechanics, vibrational analysis etc. In the following chapter the main ideas in CP2k will be presented as well as other computational methods used in the present work.

4.1 Density Functional Theory Within CP2K

The DFT calculations done in CP2K are performed using the Quickstep method [41]. Central in this method is the use of a dual basis representation for the density, called *Gaussian and Plane waves* (GPW) method. The atom centered contracted GTO basis is used to represent the KS orbitals. In contrast to the KS orbitals, the GTO basis functions are non-orthogonal, so there is an overlap between the basis functions. With the GTO basis (3.62) the density becomes,

$$\rho(\boldsymbol{r}) = \sum_{\alpha\beta} P_{\alpha\beta}\varphi_\alpha(\boldsymbol{r})\varphi^*_\beta(\boldsymbol{r}), \tag{4.1}$$

where $P_{\alpha\beta}$ is the density matrix,

$$P_{\alpha\beta} = \sum_{\alpha\beta} f_i c_{\alpha i} c^*_{\beta i}, \tag{4.2}$$

with f_i the occupation number of state i. In the framework of GTO basis set, the electrostatic Hartree energy $J[\rho]$ in (3.37) is a four-centered integral, i.e. over four basis functions, arising from the non-orthogonality. It is very costly to compute in terms of usage of memory and CPU in a computational calculation. To address this issue, an auxiliary basis

of plane waves is used to represent the density (3.67),

$$\tilde{\rho}(\boldsymbol{r}) = \frac{1}{\Omega} \sum_{|\boldsymbol{G}| \leq 2G_{\text{cut}}} \tilde{\rho}(\boldsymbol{G}) e^{i\boldsymbol{G}\cdot\boldsymbol{r}} \tag{4.3}$$

The Fourier expansion coefficients $\tilde{\rho}(\boldsymbol{G})$ are such that $\tilde{\rho}(\boldsymbol{r})$ is equal to $\rho(\boldsymbol{r})$ on a real-space grid. The fast Fourier transform (FFT) algorithm can be used to transfer the density between the reciprocal and real grid. This is exploited to solve the Poisson equation and thereby to obtain the the electrostatic Hartree energy, without the use of any expensive integration. The computation of the Hartree energy with plane wave representation scales linearly with the system size. In addition the exchange and correlation energy is calculated using the plane wave representation, while the rest of the ground state functional are treated with the GTO density.

The calculation of the ground state functional requires knowledge of the KS orbitals. As mentioned in section 3.3.2, the KS orbitals can be obtained when the Kohn-Sham equations are solved with a self-consistent method. In the GTO basis set and using a matrix formulation, the KS equations becomes a diagonalization problem. The procedure on how to solve the diagonalization problem and for the full description of the ground state energy functional, consult the original papers on Quickstep and GPW method [41, 42, 43]. CP2K also allows for the use of the orbital transfer (OT) method [44], where the KS orbitals are found by direct minimization of the ground state energy functional with respect to the KS orbital coefficients, $c_{\alpha i}$. Figure 4.1 shows a simplified flowchart on how the energy is calculated with either a traditional method involving diagonalization of the KS matrix or with the use of OT method.

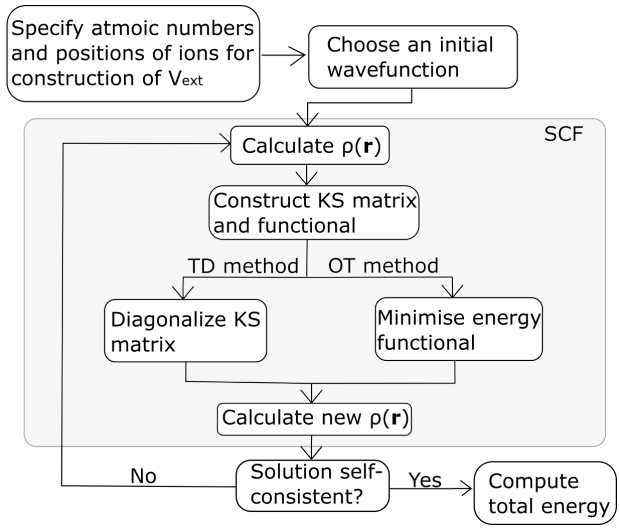

Figure 4.1: A simplified flowchart describing how to obtain the total energy with CP2K. The gray box exhibits that the density is found with a self-consistent field (SCF) method, using either the traditional (TD) method or using the orbital transformation (OT) method.

4.1.1 Periodic Calculations

An ideal crystal structures is a system of infinitely repeated unit cells in all directions. To simulate such a crystal periodic boundary conditions (pbc) are employed, where the original cell can be seen as copied infinitely in all directions. That is when for instance information is needed outside the original cell, it will collect the information from within the unit cell corresponding to that area. In CP2K pbc follows naturally when solving the Poisson equation with a FFT based method and will be employed when dealing with crystal structures.

4.1.2 Gas Phase Calculations

To study the molecules in the gas phase, single molecules were placed in a non-periodic simulation box. This corresponds physically to a low pressure(vacuum) system. This is of course a crude approximation when the environment is important part of the interactions. Furthermore, to solve the Poisson equation a wavelet solver method made available in CP2K have been used.

4.1.3 Auxiliary Density Matrix Method

In this work a few of the DFT calculations are performed using the hybrid functional PBE0. The calculation of the Hatree-Fock exchange (HFX) needed for this functional is computationally demanding for large systems described by a high quality basis set. In the CP2K framework there is a possibility to approximate the density matrix $\mathbf{P}$ with an auxiliary density matrix $\tilde{\mathbf{P}}$, called the *Auxillary Density Matrix Method* (ADMM). Excellent performances and good accuracy can still be reached with ADMM, where the approximation of HFX energy is [45],

$$\begin{aligned} E_X^{HFX}[\mathbf{P}] &= E_X^{HFX}[\tilde{\mathbf{P}}] + (E_X^{HFX}[\mathbf{P}] - E_X^{HFX}[\tilde{\mathbf{P}}]) \\ &\approx E_X^{HFX}[\tilde{\mathbf{P}}] + (E_X^{GGA}[\mathbf{P}] - E_X^{GGA}[\tilde{\mathbf{P}}]). \end{aligned} \tag{4.4}$$

The last term is a correction term computed as the difference between the density matrices using the GGA exchange functional. The auxiliary density matrix is constructed such that $\tilde{\mathbf{P}}$ is either smaller or sparser than the original density matrix, resulting in fewer HFX integrals that need to be evaluated. In this work the auxiliary basis sets provided in CP2K have been used.

4.1.4 Setup for CP2K calculations

In order to limit the size of the plane wave basis, the GTH-pseudopotentials optimized for the GGA functional PBE was used [46, 47, 48]. In addition cutoff analysis were carried out to determine the optimum E_{cut}, i.e. yielding meaningful and accurate calculations with as low E_{cut} as possible. In CP2K the default is to only perform calculations with only the Γ-point, i.e. $\boldsymbol{k} = 0$. In this work the author was only concerned with insulators and molecular systems, and thus when the cell sizes are sufficiently large, i.e. leading to small BZ volume, the default value is adequate. The Goedecker-Teter-Hutter (GTH). The

Gaussian basis set used was the molecular optimized basis set [49]. The MOLOPT basis contains several different basis set sizes, but here the Double Zeta valence with polarization functions (DZVP) have been mostly used. If a bigger basis set is used, it will be specified.

4.2 Structure optimization

In the Born-Oppenheimer approximation the nuclei move upon the potential energy surface (PES) resulting from the electrostatic energy and the kinetic energy of the electrons. Moreover, PES is a multi-dimensional function, i.e. function of the nuclear coordinates. A stable geometric structure occurs when the nuclei are located at a minimum on this surface. Generally, the surface can have multiple minima, where the first derivatives are zero and the second derivatives positive. However, in most cases the type of minimum one tries to locate is the global minimum corresponding to the equilibrium geometry.

There exists different optimization methods to find the minimum [50]. A brute force method to find the minimum would be to perform m^{3N} energy evaluations to map the PES on a grid of m points in each dimensionto. As this gives an exponential growth with system size, CP2K provides more sophisticated methods which exploits the shape of PES to determine minimas. The negative of the gradients, i.e. the first derivatives of PES with respect to the nuclei coordinates, give information on the forces acting on the nuclei. The gradients are calculated analytically, meanwhile a matrix called the Hessian containing the second derivatives $\frac{\delta E}{\delta R_i \delta R_j}$ are approximated via an updated Hessian method. The derivatives are then used to determine where the atoms should move. The applied update scheme used was the Quasi-Newton method BFGS provided by CP2k [51, 52]. Moreover, the geometry optimizations are considered converged to a minimum when the root mean square (RMS) and the maximum of the atomic forces are less than 10^{-4} atomic units. For relaxation of the crystal geometry the unit cell can also be optimized simultaneously and thus the lattice parameters might vary. For these type of calculations the optimization was considered converged when the pressure tolerance on the cell was less than 1 bar. In addition the experimental crystal symmetry was constrained in the calculation, e.g. monoclinic, orthorhombic. Besides, when performing geometry and cell optimization on crystal structures, the relative errors were calculated as

$$Err = \frac{a - a_0}{a_0}, \tag{4.5}$$

where a_0 is the experimental value and a the computed value.

4.3 Vibrational analysis

The curvature of the PES can also give information about the vibrational frequencies of the atoms. In CP2K this is done using the static-harmonic approximation. The energy (PES)

change for a displaced nucleus can be written as a Taylor expansion,

$$E(\boldsymbol{R}) = E(\boldsymbol{R}_0) + \frac{\partial E}{\partial R}(\boldsymbol{R}-\boldsymbol{R}_0) + \frac{1}{2}\frac{\partial^2 E}{\partial R^2}(\boldsymbol{R}-\boldsymbol{R}_0)^2 + \frac{1}{6}\frac{\partial^3 E}{\partial R^3}(\boldsymbol{R}-\boldsymbol{R}_0)^3 + ...$$
$$= E(\boldsymbol{R}_0) + \boldsymbol{g}(\boldsymbol{R}-\boldsymbol{R}_0) + \frac{1}{2}\boldsymbol{H}(\boldsymbol{R}-\boldsymbol{R}_0)^2 + \frac{1}{6}\boldsymbol{K}(\boldsymbol{R}-\boldsymbol{R}_0)^3 + ... \quad (4.6)$$

The third derivative is the anharmonicity $\boldsymbol{K}$, $\boldsymbol{H}$ is the Hessian, and $\boldsymbol{g}$ is the gradient. The expansion point $\boldsymbol{R}_0$ may be chosen to be a stationary point, $\boldsymbol{g} = 0$, such that the force constant matrix, i.e. Hessian, may be used to determine the vibrational frequencies, since higher order derivatives are neglected in CP2K. The 3N-dimensional Schrödinger equation (3.8) for the atoms may be transformed and divided into 3N one-dimensional Schrödinger equations, with the form of a standard harmonic oscillation [15],

$$\left[-\sum_{l=1}^{3N_{atom}} (\tfrac{1}{2}\frac{\partial^2}{\partial q_l^2} + \tfrac{1}{2}\epsilon_l q_l^2) \right] \Psi_n = E_{\mathrm{tot}}\Psi_n, \quad (4.7)$$

Where the eigenvalues ϵ_l and eigenvector $\boldsymbol{q}$, are determined from diagonalization of a mass-weighted force constant matrix. The vibrational frequencies are related to the squares of the eigenvalues. For details see refrenece [15].

As this approximation is based on a stationary point, the geometry optimization is converged with RMS forces less than 10^5 a.u. In addition threshold of $5 \cdot 10^{-}9$ on the SCF is used. From the resulting relaxed structure the vibrational analysis is carried out in CP2K, which uses finite difference method to construct the force constant matrix. The resulting vibrational frequencies are convoluted with a Lorentzian function to yield the infrared (IR) spectrum.

4.4 Population analysis

The charge and spin in a molecule or in a solid, may not necessarily be distributed evenly and have fractional charges. The atomic charges do not correspond to any unique physical property, thus the assignment of atomic charges from a DFT calculation is a mathematical way of assigning a fraction of the wave function or electron density to each atomic nucleus, called a *Population analysis*. Since there is no unique way to determine atomic charge there exists many different population techniques, e.g. Bader charge, Mulliken population, DDEC6 charge and Hirshfeld charge analysis [53, 54][55][56][57]. For this work, the Mulliken population analysis and DDEC6 charge analysis have been carried out. The Mulliken population analysis has an explicitly basis set dependence, whereas the DDEC6 partitioning scheme is independent of basis set as the charge is a functional of the total electron density distribution. Besides, the DDEC6 analysis is one of the most accurate and broadly applicable atomic population analysis methods [58]. The Mulliken population analysis is implemented in the CP2K package and gives information on both the spin and charge and is readily available. Meanwhile the DDEC6 charges were computed with the program Chargemol with the electron density computed from CP2K as input [59].

4.4.1 Bond order

Bond order is a chemical concept used to quantify bond strength and behavior, with larger bond order indicating greater strength. However, as the case with charge, it does not exist a unique way to define the bond order. The DDEC6 bond orders are based on the same DDEC6 electron density partitioning scheme and with a dressed exchange hole approach to compute the quantitative descriptors known as bond order [60, 58]. For definitions on how this is done see the mentioned papers. Moreover, the sum of bond orders (SBO) can be seen as a measure of chemical reactivity. For instance carbon prefers to share four valence electrons to get a noble electron configuration. Thus when the SBO are lower than $\sim$4, e.g. 2.58 for carbon monoxide (CO), it wants to react and form a molecule where its SBO is $\sim$4, like in the CO_2 molecule [60]. The DDEC6 bond order has several advantages compared to other bond order definitions, for instance it does not break down for longer bonds, as seen in bonding/antibonding definition and assumptions of constant bond orders with respect to density overlap [61]. The DDEC6 bond order has also some reported areas where it does not work, though none which are important for this work, e.g. it does not apply for extremely high-energy excited states, electrides and highly-dependent states.

The bond orders are computed with the same Chargemol program.

4.4.2 Determination of Copper Oxidation

A recent study compared DDEC6 charges with Bader charge analysis for different crystal structures and molecular systems [62]. They found that the charges for the two methods are in close agreement. In addition they did DDEC6 charge analysis on several different known Cu(II) and Cu(I) complexes with different combination of anionic and neutral ligands. The result is listed in table 4.1. These results will be used to compare with DDEC6 charges calculated here in order to determine the oxidation state of Cu.

Table 4.1: Results from an earlier study where known Cu(I) and Cu(II) complexes are modeled using the DDEC6 charge population analysis[62]. The table shows the relationship between the Cu oxidation states and the average DDEC6 charge as well as the range of charges.

Oxidation state	Average charge (e)	Range
Cu(I)	0.85 $\pm$0.17	0.44 - 1.1
Cu(II)	0.36 $\pm$0.08	0.25 - 0.52

4.5 Dispersion Correction

Weak interactions arising from instantaneous dipoles, i.e. London dispersion forces are not properly described in standard DFT [15, 63]. This interaction is important for instance in binding between rare gasses and on a longer scale, as a intermolecular force. The missing dispersion energy E_{disp} can be accounted for by adding it to the energy, E_{DFT}, from the SCF procedure ,

$$E_{\mathrm{DFT-D3}} = E_{\mathrm{DFT}} - E_{\mathrm{disp}}. \tag{4.8}$$

In CP2K the Grimme D3 method is made available and has been used in parts of this work. For the definition of E_{disp} for the Grimme D3 method see the original paper [64]. The dispersion correction have been shown to give good results for noncovalent interactions in gas phase system and in molecular crystals [64, 65].

4.6 Bond stretching and bond dissociation energy

To get more insight in how stable a molecule or bond is, one can in addition to the bond orders, look at the energy required to stretch the bond. To stretch a bond between molecule(s) and/or atom(s) A and B, the bond stretching is performed by translating the molecule or atom B by a small deviation δ_b and performing a DFT calculation to get the energy. The DFT calculations can either be performed as a single energy evaluation at each step of the stretch or one can relax the geometry if the atom/molecule is fixed in space.

If one stretches the bond to infinitely, i.e. in practice until the Coulomb interactions are insignificant, the energy difference between the ground state and last step of the stretch converge to the bond dissociation energy for a non-vibrating molecule. The bond dissociation energy required to break a bond through the reaction

$$AB- > A + B, \tag{4.9}$$

is then defined for the non-vibrating case as,

$$D = E(A) + E(B) - E(AB). \tag{4.10}$$

However, a quantum mechanical system is constantly fluctuating, even at zero Kelvin. The energy of this small residual motion at zero kelvin is the *zero-point vibrational energy* (ZPE) and can be quite accurately approximated by harmonic oscillators [15]. The ZPE is then just half of the sum of the fundamental vibrational frequencies ν_i [66],

$$ZPE = \frac{1}{2} \sum_{i=1}^{N_{\mathrm{atom}-6}} \nu_i. \tag{4.11}$$

For a nonlinear molecule of N_{atom} atoms there are $3N_{atom}$-6 vibrational frequencies. The vibrational frequencies determined from HF and DFT methods have been observed to have a tendency to be larger than the experimental values. A common practice is therefor to compensate this by multiplying with a scale factor [67]. Sources of errors to the vibrational frequencies may be for instance the neglecting of anharmonic effects and finite basis set size. The bond dissociation energy can then be corrected by the inclusion of the ZPE. This correction corresponds to the bond dissociation energy at 0 K, and becomes

$$D_0 = E(A) + ZPE(A) + E(B) + ZPE(B) - E(AB) - ZPE(AB). \tag{4.12}$$

When performing vibrational analysis in CP2K, it is also possible to get information about the thermal corrections at finite temperatures due to the vibrational motion, as well as contributions from rotational motion and translation. Instead of adding the ZPE one can then instead add thermal enthalpy correction given by CP2K to give the bond dissociation enthalpy.

4.7 Molecular Dynamics

In the aforementioned theory on electrons and nuclei, the system was treated without time dependency. It is however also of interest to study how the particles behave with respect to time, not only at a microscopic level, but also at a macroscopic level. These two branches can be connected with statistical physics, i.e. deriving the thermodynamic properties from statistical ensemble [68]. To this end ab intio Born-Oppenheimer (BO) MD simulations have been performed to obtain the ensemble average. The *ergodic hypothesis* connects the ensemble average to the time average [15],

$$\langle X \rangle = \lim_{\tau \to \infty} \frac{1}{\tau} \int_0^\tau X(t) d\tau = \lim_{K \to \infty} \sum_{i=1}^{K} X(t_i) \tag{4.13}$$

Here $\langle X \rangle$ is a macroscopic observable, that is the time average of the instantaneous state X(t). The number of times the system is sampled in a MD simulation, K, should be large for accurate results [69].

Moreover, in BO MD the ions are treated as classical particles moving in a potential V, where the equation governing the motions of the ions is Newtons equation [36],

$$M_i \frac{d^2 \boldsymbol{R}_i}{dt^2} = -\frac{dV(\boldsymbol{R})}{d\boldsymbol{R}_i}, \tag{4.14}$$

where the resulting energy from the static DFT calculation is the potential,

$$V(\boldsymbol{R}) = \min_{\phi} [E_{\mathrm{KS}}(\{\phi_i(\boldsymbol{r})\}; \boldsymbol{R})]. \tag{4.15}$$

To find how the particles move dynamically one then needs to integrate the equation (4.14) with respect to time. From a computational view point this is a problem of discretization of time. How to go from one discreet time step to another is called the integrator. In this work a ASPC integrator have been used with extrapolation order of three, that is for each step in MD an extrapolation from the three previous converged wave-functions are used [70]. Furthermore, the MD simulations was done with a canonical ensemble, that is with a constant volume, particle numbers and temperature. A canonical ensemble is in contact with a heat bath, and likewise during the simulations energy fluctuations are generated with a external bath. This is called a thermostat, and for this work a CSVR thermostat have been used with time constant of 2000.

Chapter 5

Results and Discussion

This chapter includes presentation and discussion of the results.

5.1 Convergence Tests

As mentioned in the previous chapter, the software CP2K uses a dual basis representation, with the electron density and Gaussian functions represented on real space grid(s). Having a good enough resolution of this grid is crucial for obtaining accurate and meaningful results. What determines this resolution is the plane wave cutoff defined in section 3.4.2. The result of the convergence test for $Cu[HCOO]_2$ in the gas phase is shown in figure 5.1. The first graph shows single total energy evaluations of the Cu molecule as a function of the cutoff energy. The calculations are in general considered converged when the energy deviates less than $\pm$ 0.2 kcal/mol from the last value. On a general basis, one is concerned with energy differences and not the total energy. Thus a better measure is a convergence test based on the the dissociation energy, equation (4.10) with a non-relaxed geometry. This convergence test tend to converge more rapid than the former because of systematic error canceling. For instance, the given convergence criteria is satisfied with a cutoff value of 470 Rydberg (Ry) or higher, while the binding energy can be observed to have the same accuracy already at 350 Ry.

Table 5.1: Shows the obtained values of plane wave cutoff E_{cut} and relative plane wave cutoff E_{rel} for different systems.

(a)

Cu-crystal	E_{cut} [Ry]	E_{rel} [Ry]
$[HCOO]_2$	510	55
$(pyr)_2[HCOO]_2$	480	55
$(en)_2[HCOO]_2$	420	55

(b)

Cu-molecule	E_{cut} [Ry]	E_{rel} [Ry]
$[HCOO]_2$	510	55
$(pyr)_2[HCOO]_2$	430	51
$(en)_2[HCOO]_2$	430	51

With the change of basis, introduction of new elements or with different crystal structures a new cutoff value was found. In table 5.1 the different cutoff values are tabulated together with the relative cutoff parameter. This parameter is tuned in the same manner as the cutoff, for instance in Figure 5.2 the convergence test for the cutoff and relative cutoff is shown for the Cu(en)$[HCOO]_2$ crystal structure.

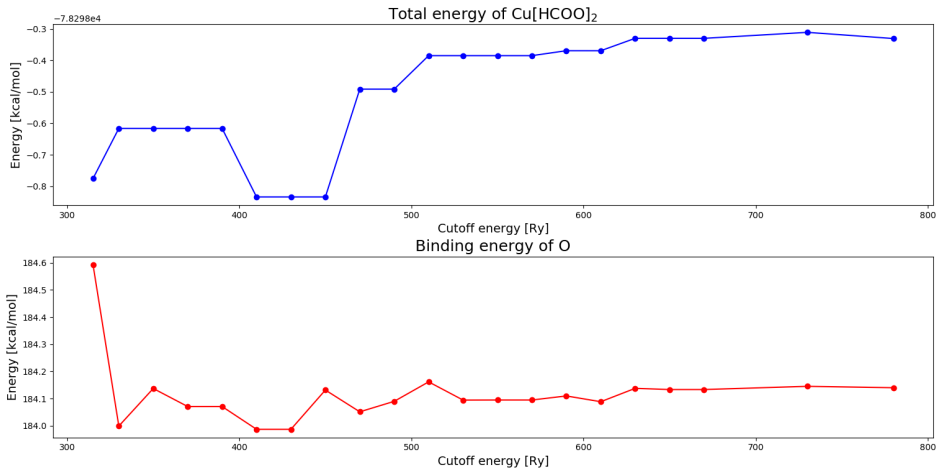

Figure 5.1: The first plot is the total energy of the $Cu[HCOO]_2$ molecule, while in the second plot the binding energy of oxygen is calculated.

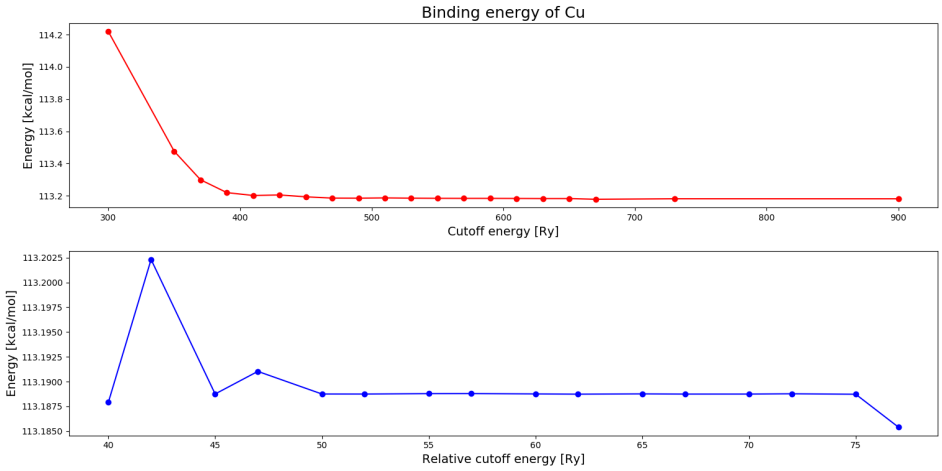

Figure 5.2: The results from the cutoff calculations done on the $Cu(en)_2[HCOO]_2$ crystal structure. In the first plot the binding energy is plotted against the Cutoff energy, while in the second against relative cutoff energy.

5.2 Gas Phase Calculations

The three different molecules, $Cu[HCOO]_2$, $Cu(en)_2[HCOO]_2$ and $Cu(pyr)_2[HCOO]_2$ have been studied in the gas phase. For the calculation of the bond dissociation energy of the molecule [HCOO] one would require the energy of its optimized structure. therefore calculations have been performed for the HCOO molecule as well, and these results will be presented first.

5.2.1 Formate Neutral Radical

The formate neutral radical HCOO was placed in a cubic box with $a = 20.0\,\text{Å}$ and with a cutoff value of 510 Ry. Previously optimized structure of the radical was used as a starting structure for the geometry optimization taken from the NIST database [66]. In addition the spin state is reported to be in a doublet state, $<S^2> = 0.75$, therefore this spin configuration is used. For curiosity other starting structures were used as well, and notably a geometry with lower energy than the reported ground state structure was found. In this case the coordinates of the formate anion $HCOO^-$ was used as a starting point for the geometry optimization, and the resulting favorable energy was 0.89 kcal/mol. This shows that the level of theory used in this thesis, i.e. DZVP bais set, PBE XC functional and GTH pseudopotential, is not reliable when energy differences become closer than at least 1 kcal/mol. Which is also understandable from the cutoff convergence criteria. The results of the formate neutral radical, as well as the formate anion is given in table 5.2.

Table 5.2: The results of DFT calculations done on the reported ground state (GS) formate neutral radical and the structure geometry of the radical giving the lowest energy (LE) in this work.

	This work		NIST database [66]	
	LE HCOO	GS HCOO	PBE/6-311G**	B3LYP/6-311G**
		Bond length (Å)		
CH	1.560	1.103	1.108	1.099
CO	1.238	1.266	1.262	1.251
		Bond angle (°)		
OCO	108.15	112.95	113.24	113.11
		Zero-point energy (kcal/mol)		
ZPE	10.86	12.30	11.93	12.41

The result shows that the vibrational analysis and geometry optimization done on the reported ground state, HCOO molecule reproduces well the values given in the literature [66]. Moreover, the corresponding literature values listed in the table is based on a higher level of theory. Namely all electron calculations with the hybrid functional B3LYP and all electron calculation with PBE functional, which is believed to be more accurate. All in all the results are acceptable, as there is a trade off between accuracy and computational speed, but one should keep in mind that when the energy difference between two isomers is small, one cannot determine the minima.

5.2.2 Copper Formate

The $Cu[HCCO]_2$ molecule was placed in a cubic $a = 15.0\,\text{Å}$ box. There was found no mention of the geometry of this molecule in the literature. So in order to determine the ground state, one has to search through different structural isomers and see which configuration yields the lowest energy. In addition the spin multiplicity of the molecule is unknown. The molecule HCOO only needs one electron to fulfill its shells and become the favourable formate anion. Moreover, the molecule is an anion in solution, so one can therefore suspect that the Cu should be found in a Cu(II) charge state, with electron configuration $[Ar]3d^9$, i.e. a spin doublet state. And since the formate anion is in a singlet state [66], the spin multiplicity of the $Cu[HCOO]_2$ is suspected to be in a doublet state. To be sure of this, the different isomers were also tested with quartet state, i.e. spin multiplicity of 4. These states showed a consistently higher energy, and thus it is concluded that the molecule is in a doublet state. Higher spin states, e.g. 6, 8, .., are not considered as this would mean that the electrons are promoted to higher and higher energy orbitals, which is not favorable. The optimized geometry of the different isomers tested is shown in Figure 5.3. Vibrational analysis on the configuration marked as "Ground state" gave only real valued frequencies, which confirms that this structure is at least a minimum on the PES. Furthermore, the energy differences between the two most energetically favorable states are significant (15.8 kcal/mol), thus it is safe to infer that this is the ground state structure. Moreover, the energy increases from A to E and thus it is observed that Cu prefers to be in a four coordinated square planar geometry.

Population analysis

The result of the population analysis of the ground state shows that the Cu atom has a charge of +0.87e. From the method section 4.4.2, this value is very close to the average value of Cu species with formal charge Cu(II). It therefore looks indeed like each formate gets the desired electron. The bond orders and charges are given in table 5.3.

Table 5.3: Results from the DDEC6 charge and bond order analysis. Table (a) contains the average bond order with standard deviation for the bonds in the $Cu[HCOO]_2$ molecule. Table (b) contains the sum of bond orders and charges.

(a)

Bond	bond order
Cu-O	0.43 ± 0.016
Cu-C	0.09 ± 0.002
C-O	1.61 ± 0.006
C-H	0.84 ± 0.001

(b)

Element	Sum of bond orders	Charge (e)
Cu	1.91	0.87
O	2.17	-0.48
C	4.16	0.45
H	0.91	0.08

The bond order between Cu-O is significantly smaller than the C-O, indicating that this bond may be of more ionic character than covalent, which supports the charge transfer from Cu to the $[HCOO]_2$ molecules. The sum of bond orders (SBO) of carbon and hydrogen is $\sim$4 and $\sim$1 respectively. This is consistent with carbon sharing 4 electrons and hydrogen 1 electron in covalent bonding to be in octet state.

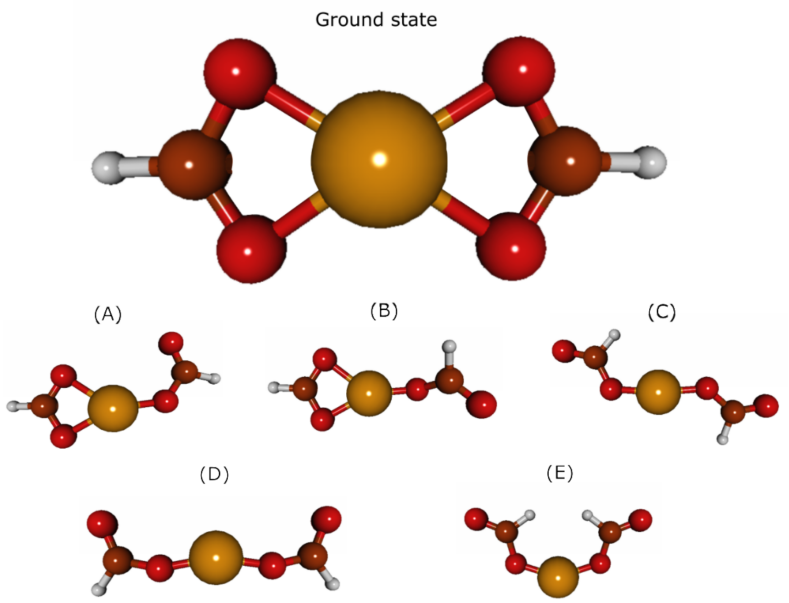

Figure 5.3: The color scheme indicates different atoms; orange for copper, red for oxygen, brown for carbon and white for hydrogen. Energy of different isomers of $Cu[HCOO]_2$ were computed to find the structure yielding the lowest energy, i.e. the ground state. The energy difference between the ground state and the other isomers are from A to E: 15.8, 18.7, 36.0, 38.0 and 41.8 kcal/mol.

Copper formate

To get a better idea on how strong the bond between the Cu and formate is, the bond dissociation energy needs to be computed. However, this calculation requires the energy of the oligomer Cu[HCOO]. This structure and spin state is also unknown. The two configurations shown in Figure 5.4 have been tested with 1, 3 and 5 spin multiplicities. The configuration (B) in a singlet state was the most favorable with 10.32 kcal/mol lower in energy than the next lowest structure. This shows yet again that it is preferable that both oxygen is coordinated to the Cu. The DDEC6 charges give Cu a charge of +0.46e, which is in the upper region of the Cu(I) states (see 4.1).

Bond dissociation energy

The bond dissociation energy can than be computed based on the $Cu[HCOO]_2$, Cu[HCOO] and [HCOO] calculations summarized in table 5.4. These values are results from geometry optimization and vibrational analysis.

The resulting bond dissociation energies calculated from equation (4.10) and (4.12) is given in table 5.5. The thermal vibrations lead to lower bond dissociation energies, but the values are still high and this indicates that the bond is quite strong.

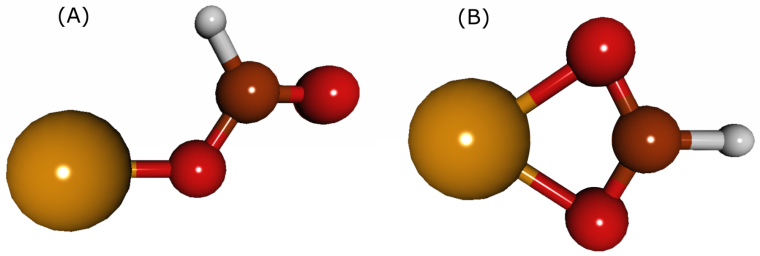

Figure 5.4: The two different configurations of the Cu[HCOO] molecule tested. Configuration (B) was found to be the ground state with 10 kcal/mol lower in energy than configuration (A).

Table 5.4: The results from geometry optimization gives the total energy E_{tot}, while the zero-point energy (ZPE) and the enthalpy correction H_{corr}(298K) at 298 K are from the vibrational analysis.

Molecule	E_{tot} [kcal/mol]	ZPE [kcal/mol]	Hcorr(298K) [kcal/mol]
[HCOO]	-24012.97	12.30	14.51
Cu[HCOO]	-54205.73	14.09	16.95
$Cu[HCOO]_2$	-78298.85	31.38	35.42

Table 5.5: The bond dissociation energies of the formate bond are calculated with different schemes. The uncorrected bond dissociation energy is denoted D, while D_0 denotes the bond dissociation energy at 0 kelvin and $DH^\circ{}_{298}$ the bond dissociation enthalpy at 298K.

Bond dissociation energies		
D [kcal/mol]	D_0 [kcal/mol]	$DH^\circ{}_{298}$ [kcal/mol]
81.16	76.17	77.2

5.2.3 Copper Pyridine Formate

A four-step decomposition of the crystal $Cu(pyr)_2[HCOO]_2$ upon heating was previously found in another study and presented here in Figure 2.2 [3]. From the first to the second step one of the coordinating pyridine evaporates and the resulting structure forms a $Cu_2(pyr)_2$- $[HCOO]_2$ dimer. This intermediate Cu(II) complex shows great structural resemblance to the third step of the reduction pathway, namely the Cu(I) intermediate. The study concluded that the high structural resemblance between the Cu(II) complex and Cu(I) complex, and that the Cu(I) intermediate is relative stable, results in a low reduction temperature.

Furthermore, Marchal et al. deduced the structure of the intermediate Cu(II) and Cu(I) complex from Extended X-Ray Absorption Fine Structure (EXAFS) measurements [3]. Since the intermediate crystal structures Cu(II) and Cu(I) consist of discrete units of $Cu_2(pry)_2[HCOO]_2$, these complexes were used as a starting point for the geometry optimization. This was done in order to get more insights about these molecules in the gas phase. To simulate the gas phase, single molecule calculations were performed in a

$a = 20$ Å box. For the Cu(II) complex the spin multiplicity of the molecule is unknown, therefore simulations with spin multiplicities 1, 3 and 5 were performed. It was found that the singlet state was more favorable than the triplet and quintet state with 1.3 kcal/mol and 77.6 kcal/mol respectively. As previously discussed one can not determine if the singlet or triplet state is the ground state based on such small energy differences. Moreover, the geometry of these two are practically the same as can be seen from some selected bonds in table 5.6 (a).

Table 5.6: Selected average bond length and bond angles for the $Cu_2(py)_2[HCOO]_2$ molecule is found in part (a) of the table. The charges in part (b) are from DDEC6 charge analysis, and the spin moments are from Mulliken population analysis.

	Singlet	Triplet
Bond length (Å)		
Cu-N	2.19	2.20
Cu-O	2.03	2.03
Bond angle (°)		
N-Cu-O	94.95	95.47
Cu-N-C	120.86	120. 89

(a)

Element	Charge	Spin moment
Singlet state		
Cu	0.84	$\pm$ 0.66
O	-0.52	$< \pm$ 0.09
Triplet state		
Cu	0.84	0.66
O	-0.52	$<$ 0.09

Part (b) of the table shows results from DDEC6 and Mulliken population analysis. The charges are from DDEC6 analysis, while the spin moment, i.e. difference between α-spin and β-spin, is obtained with Mulliken analysis. It can be observed that the charges are the same with Cu in the correct oxidation state Cu(II). Since Cu formally is in the Cu(II) state, it is expected to be one electron short in the d-shell, i.e. spin moment around 1. The calculated spin moments supports this idea since in both cases it was optimal to have the same absolute spin moment of 0.66. For a singlet state the sum of individual atom spin moments are zero, hence the two Cu's have opposite sign, whereas the triplet state has parallel spins. The rest of the elements have small fractional spins with oxygen having the highest spin moment of the non-Cu atoms. As mentioned, with the current setup it is not possible to find out if the ground state prefers parallel or anti-parallel spins. However, as both configurations have the same geometry, charges and almost equality in energy, it is assumed that the strength of the bond is of equal strength. therefore probing the strength of the formate bond will be performed for the singlet state.

Probing the Formate Bond

As a first inspection of the strength of the formate bond, one can look at the energy needed to stretch the formate molecule, given in Figure 5.5.

Only single-point energy evaluations were performed at each step of the stretch, with the converged wavefunction from the previous step as a starting guess for the SCF procedure. This ensures that the spin-states carry over to the next step, or at least is probed in the SCF procedure. Since the new geometry with the stretched formate is no longer a ground state, the SCF method might have converged to another minimum. It is also benefit that it saves computational resources.

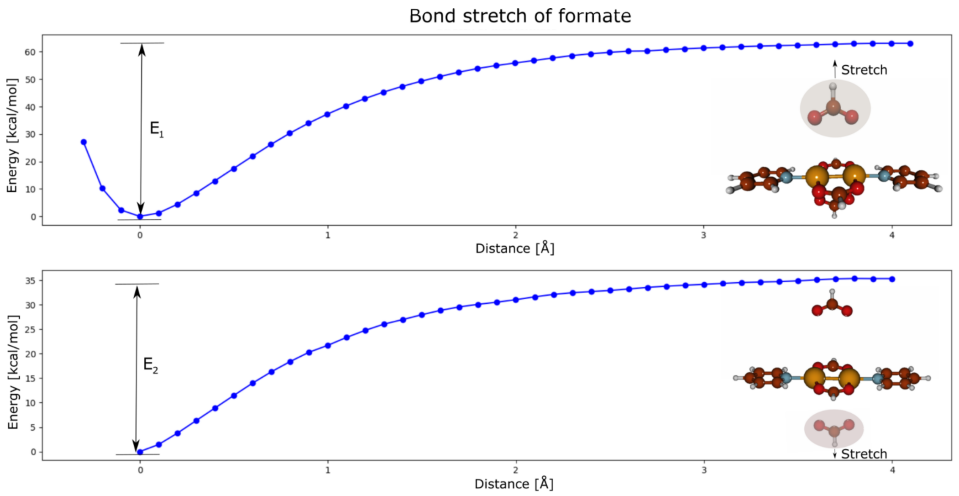

Figure 5.5: The energy E_1 required to stretch the first formate is shown in the first plot, and in the second plot the second formate is stretched. The color scheme of the atoms are as follows: orange for copper, red for oxygen, white for hydrogen, brown for carbon and blue for nitrogen.

The energy required to stretch the first formate, E_1, should be close to the energy required to break the bond, as mentioned in section 4.6. Because of the long range Coulomb interaction, the negative formate will always interact with the Cu-molecule. From the Figure it is observed that at 4 Å this becomes quite negligible. The sum of energies E_1 and E_2 is $E_{\text{stretch}} = 94.4$ kcal/mol. In this case the formates where pulled perpendicular to the pyridine plane. Geometry optimization simulation was performed with the formates pulled parallel and 5.14 Å from the Cu centers. The geometry relaxed back to the configuration with the pulled formates perpendicular to the pyridine plane and the bonded formates parallel to the plane. therefore the first inspection shows that it requires 47.2 kcal/mol for each Cu atom to break the formate bonds and form the Cu(I) structure.

DDEC6 charges

The ground state of the $Cu_2(pyr)_2[HCOO]_2$ molecule is depicted in Figure 5.6 together with the resulting DDEC6 charges. When two of the formates are 5.14 Å from the Cu centers the new charges are found and shown in part (b) of the Figure. The Cu in the ground state has a charge corresponding to the Cu(II) oxidation number. In part (b) of Figure 5.6 however, it is observed that Cu has a DDEC6 charge of 0.44e. When comparing with table 4.1, one observes that the charge is in the upper range of the interval, but still within the standard deviation of the Cu(I) states.

Under thermal curing, the formate decomposes to gaseous products, whereupon an electron transfers to the Cu, i.e. a reduction of Cu(II) $\rightarrow$ Cu(I) [3]. It is observed from Figure 5.6 that the charge transfer may not have undergone yet, as the molecule [HCOO] is still negatively charged. The energies E_1 and E_2 is a measure on how strong the formate bond is, albeit it does not capture the whole picture. It is therefore thought that the energy

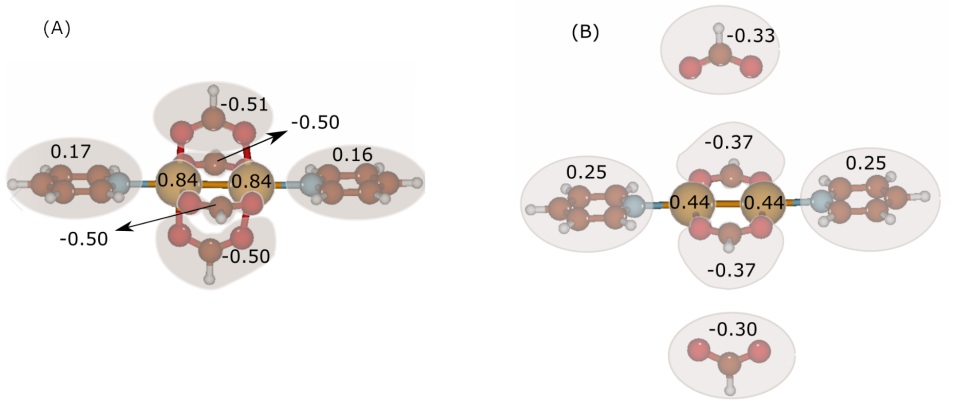

Figure 5.6: The calculated DDEC6 charges for pyridine, formate and the Cu atoms are displayed. Part (A) of the figure is the ground state of the $Cu_2(pyr)_2[HCOO]_2$ dimer and (B) is the relaxed geometry when the formates have been stretched 5.14 Å.

should be seen together with the bond dissociation energy. This energy is calculated from the energy difference between the ground state, $Cu_2(pyr)_2[HCOO]_2$, and the products [HCOO] and $Cu_2(pyr)_2[HCOO]$. That is, the formate neutral radical is used instead of the formate anion.

Intermediate Cu(I)

As mentioned, the intermediate Cu(I) structure is known and is shown together with the DDEC6 charges in Figure 5.7. Once again the spin state is unknown, but the electron configuration for Cu(I) atom is $[Ar]3d^{10}$, so it is expected that it is a closed shell molecule. The energy difference between the singlet and a triplet state of this molecule is 148.9 kcal/mol in favor of the singlet. It is therefore safe to conclude that it is preferable with zero spin moments, i.e. singlet state.

Comparing the charges of the Cu centers with table 4.1, it is observed that this time the charges are in the lower region of the Cu(I) interval. Although, keep in mind that there is an electron transfer under thermal decomposition of the formate, thus it is expected to be lower than when the formate is only stretched.

The Cu(II) complex has a coordination number of 6 in a distorted octahedral geometry, which is typically found for d^9 Cu(II) systems [13]. Cu(I) has a formal d^{10} metal center, which is generally found in a tetrahedral geometry. However, from Figure 5.7, one can see that it adopts a distorted square planar geometry. This is not a common geometry, but there are incidence when a formal d^{10} or a Cu(I) complex is found as a square planar or distorted square planar geometry [71, 72]. Furthermore, the bond order of some selected atoms are presented in table 5.7. There is an increase in covalent character for the coordinated atoms when going from a Cu(II) to Cu(I) complex, and the SBO for Cu in the two cases are 2.25 and 2.16 respectively. This indicates that the remaining coordinated molecules got a stronger bond in the Cu(I) complex.

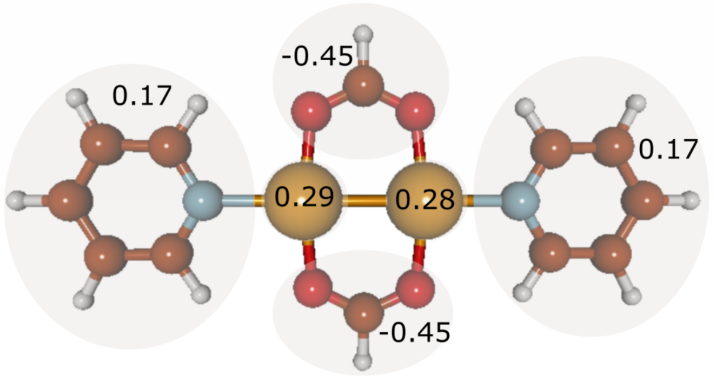

Figure 5.7: The Cu(I) ground state structure with computed DDEC6 charges.

Table 5.7: Selected bond orders for the $Cu_2(py)_2[HCOO]_2$ molecule and the intermediate Cu(I) structure $Cu_2(py)_2[HCOO]$.

Bond	Cu(I) complex	Cu(II) complex
Cu-O	0.61	0.41
Cu-N	0.47	0.32
Cu-Cu	0.28	0.11

Bond dissociation energy

The bond dissociation energy of the two formates from the Cu(II) complex can than be computed based on the previous data on [HCOO] in table 5.4 and the energies of the Cu-Pyridine complexes. The energies of the Cu-Pyridine complexes can be found in table 5.8.

Table 5.8: The results from geometry optimization gives the total energy E_{tot}, while the zero-point energy (ZPE) and the enthalpy correction $H_{corr}(298K)$ at 298 K are from the vibrational analysis.

Molecule	E_{tot} [kcal/mol]	ZPE [kcal/mol]	Hcorr(298K) [kcal/mol]
$Cu_2(pyr)_2[HCOO]$	-208545.32	179.22	192.83
$Cu_2(pyr)_2[HCOO]_2$	-160407.34	145.11	156.45

The resulting bond dissociating energies are given in table 5.9. The non-vibrating value, D, is almost 20 kcal/mol higher than what was found by the stretching the formate. In general these values should converge to the same value when the formate is stretched sufficiently far, but given that the stretch is performed with single-evaluations and the fact that the formate retains its negative charge, it is natural that they deviate.

Table 5.9: The bond dissociation energies of two formate bonds are calculated with different schemes. The uncorrected bond dissociation energy is denoted D, while D_0 denotes the bond dissociation energy at 0 kelvin and DH°_{298} the bond dissociation enthalpy at 298K. The energy required to stretch the bonds is given as $E_{stretch}$

Bond dissociation energies			
D [kcal/mol]	D_0 [kcal/mol]	DH°_{298} [kcal/mol]	$E_{stretch}$ [kcal/mol]
114.05	79.94	77.68	94.4

5.2.4 Ethylenediamine

The crystal structure of Cu formate complexes coordinated by ethylenediamine (en) ligands, are built up of units of $Cu(en)_2[HCOO]_2$ molecules. For the gas phase calculations such a molecule was placed in a 20 Å box. From Figure 2.2 we know that the reduction temperature is higher compared to the Cu pyridine complex. Marchal et al. proved that a unstable intermediate Cu(I) does exists, however the structure is based on indirect measurements and literature [3]. Moreover, the increase in reduction temperature is believed to be due to an energetically unfavorable intermediate on the reduction pathway that needs to be surpassed.

The $Cu(en)_2[HCOO]_2$ molecule was relaxed with spin multiplicity 2 and 4. The low spin state yielded 80 kcal/mol lower energy and is depicted in Figure 5.8. The result of the

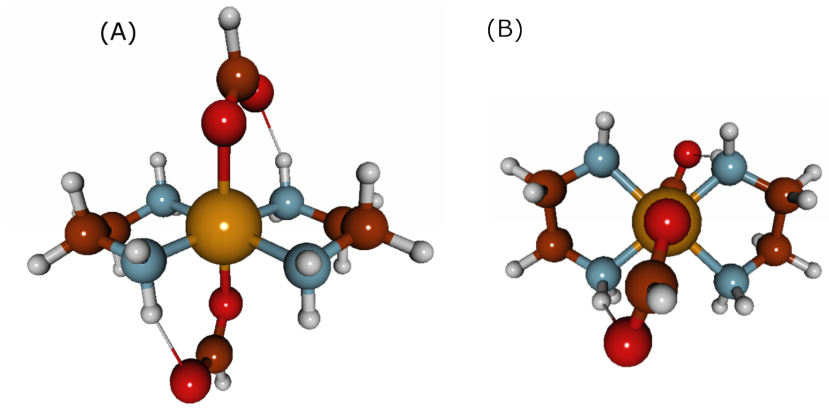

Figure 5.8: The $Cu(en)_2[HCOO]_2$ molecule as depicted from two different angles in (A) and (B) respectively.

DDEC6 population analysis can be found in table 5.10. The oxygen not coordinated to the Cu has a charge of -0.58 and a small bond order to one of the hydrogen with a charge of 0.29. This indicates that a hydrogen bond is formed [60]. It has previously been observed a correlation between the ability to form hydrogen bonds between the amine and formate ligands and the reduction temperature [8]. Moreover, it was argued that the reduction temperature is effected by steric hindrance. All the hydrogen bonded to the nitrogen have DDEC6 charges of 0.29, and hence have the ability to form hydrogen bonds. No further

Table 5.10: Results from the DDEC6 charge and bond order analysis for the $Cu(en)_2[HCOO]_2$ molecule. Table (a) contains the average bond order for selected atoms. The oxygen which is not coordinated to the Cu is denoted by an asterisk. Table (b) contains the DDEC6 charges.

(a)

Bond	bond order
Cu-O	0.22
Cu-N	0.44
O^*-H^*	0.15

(b)

Atom/Molecule	Charge
Cu	0.80
Formate	-0.74
Ethylenediamine	0.33

investigation on this topic has been made herein.

Meanwhile, the bond order to the coordinated oxygen is weak (0.22), but the formate is more negatively charged than in the Cu pyridine complexes, thus displaying a more ionic character. How this effect the strength of the bond will be probed by stretching the formate.

Stretch of the formate

The energy required to stretch the formate is plotted in Figure 5.9. One can observe that when the formate is stretched 6.8 Å from its equilibrium position, it requires $E_{\text{stretch}} = 55.56$ kcal/mol. The DDEC6 charge analysis was done on a relaxed geometry where the formate was located 8.5 Å away from the Cu center. The aim behind this calculation was to see if there was any indication of charge transfer. The Cu center had a calculated charge of 0.50, which is on the boundary between the Cu(II)/Cu(I) states (see table 4.1). However, the formate is still largely negatively charged (-0.54), and therefore just the stretch of formate cannot be seen as a charge transfer mechanism, i.e. in accordance with previous section 5.2.3.

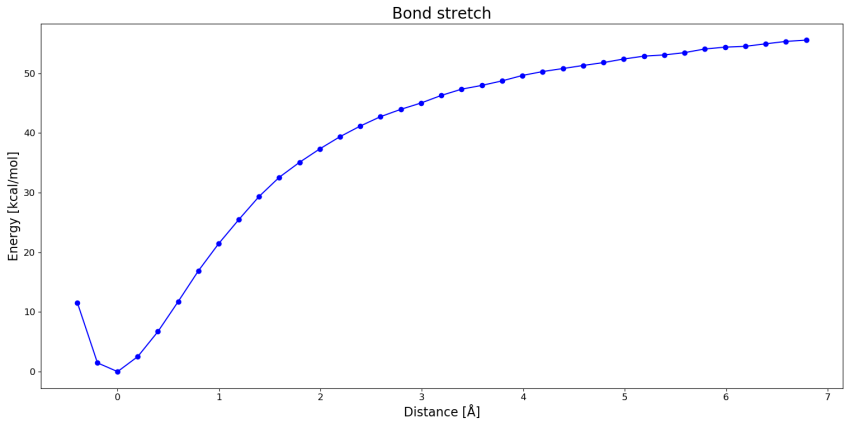

Figure 5.9: The energy required to stretch one of the formates in the $Cu(en)_2[HCOO]_2$ molecule is plotted against the distance from the equilibrium bond position.

The result of the stretching in the $Cu_2(pyr)_2[HCOO]_2$ case, was that ~ 94.4 kcal/mol is required to remove two formates. Comparing $2E_{\text{stretch}} = 111.2$ kcal/mol with this value, it is observed that the formate bond for the $Cu_2(en)_2[HCOO]_2$ molecule is weaker. This could be a part to why the reduction temperature for the Cu(en) complex is lower than the Cu(pyr) complex. However, the data set is too small to conclude, and other Cu formate based MOD inks should be tested first. Nonetheless, the present finding is worth to keep in mind.

Intermediate

The exact structure of the Cu(I) intermediate has not been proven. Figure 5.10 shows different relaxed configurations. A relaxed geometry with both the ethylenediamine as a bidentate ligand was not found. In a recent study one found a correlation between ligand

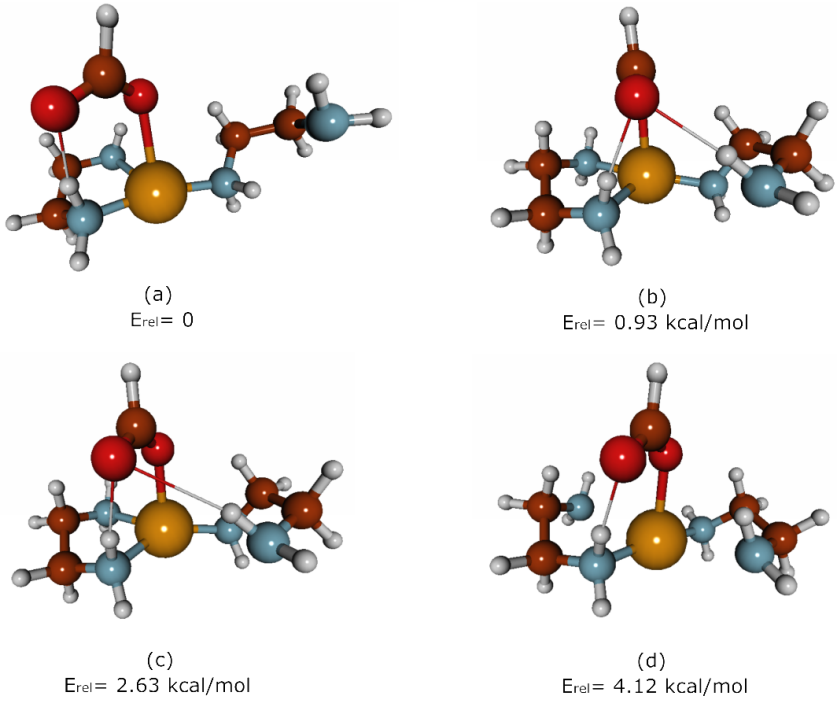

Figure 5.10: Different configurations of the Cu(I) ethylenediamine complex have been relaxed. The relative energy between the configurations are marked as E_{rel}.

denticity and protection against oxidation in the Cu MOD inks [73]. It was demonstrated that monodentate ligand class complexes had a more pronounced Cu_2O formation than the bidentate class complexes. The Cu_2O formation can impede the conductivity, therefore it is of importance whether the Cu(I) and Cu(II) complexes form bidentate structures. As can be seen from Figure 5.10 there are small energy differences between the structure, and one can observe that the difference in geometry lies in the formation of hydrogen

bonds in part a, b and c. They also exhibit a four coordinated complex which looks like a distorted tetrahedral geometry. From the energy differences it is not completely safe to conclude which of the structures (a) and (b) are the most optimal. One can also rule out the monodentate structure (d). However, the DDEC6 charges for structure (a) yield a charge of 0.20 which is outside the interval of the Cu(I) complexes in table 4.1. This indicates that we have not found the ground state intermediate structure and it should be investigated further.

5.3 Crystal Structures

The experimental crystal structures was used as a starting point for the anhydrate $Cu[HCOO]_2$, $Cu(en)_2[HCOO]_2$ and $Cu(pyr)_2[HCOO]_2$ calculations. The experimental unit cell was taken from the the Cambridge Crystallographic Data Centre [74]. As mentioned in section 4.1.1, pbc are applied for all crystal calculations.

5.3.1 Copper Formate

Many properties that can be calculated from DFT on crystalline materials require a relaxed geometry and lattice parameters [40]. The reason is that DFT calculations are not exact and does not necessary capture exactly the forces at play. Another equilibrium is therefore found, albeit the geometry should be close to the experimental. Figure 5.11 shows the crystal structure, with its orthorhombic unit cell replicated in the the lattice directions a_2 and a_3 . Each Cu is 5 coordinated in a distorted tetragonal-pyramidal geometry. The oxygen in the formate group are covalent bonded to the Cu atoms, making a bridging network between the Cu atoms. Further discussion on the crystal structure can be found in [75].

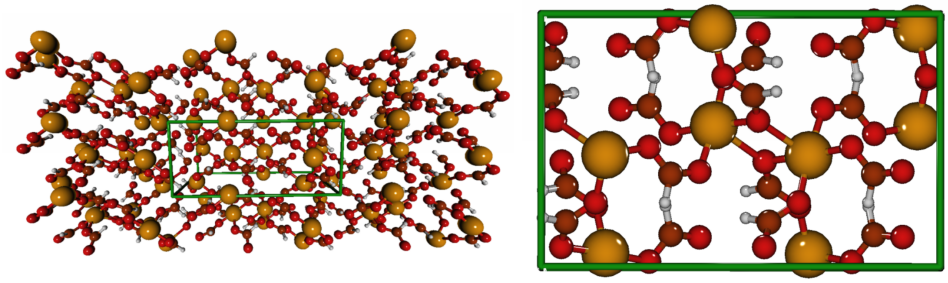

Figure 5.11: The crystal structure of $Cu[HCCO]_2$. Left sides shows the unit cell repeated in a_2 and a_3 direction, while to the right the a_2-a_3 plane is depicted with the sole unit cell.

The optimization of the geometry and lattice cell vectors where done with different plane wave cutoffs to check if the geometry is well behaved with respect to the cutoff. The relaxed structure was compared with selected experimental bond lengths, volume, bond angle and lattice vectors. The experimental values can be found in table 5.11 together

with the computed values. The bond lengths and the bond angle listed in the table were measured between the same atoms and the superscript defines between which atoms in accordance to Figure 5.12. Since the lattice parameter in the a_3 direction is just $6.2\,\text{Å}$, a test was done to check if sampling at the gamma point is sufficient. Simulations done with more k-points or equivalently increasing the real space lattice, hence denser k-space, would give more accurate results if this was a problem. Repeating the unit cell results in doubling of number of atoms, so to decrease the computational cost a short range (SR) basis set was used, i.e. basis set with fewer diffuse primitive Gaussian functions. From table 5.11 one can observe that this approximation for the single unit cell case, did not perform any worse than its counterpart. In the case of multiple unit cell in the a_3 direction, the results show that it does not consistently perform better than single cell calculations and thus the gamma point is adequate.

Table 5.11: The experimental data is taken from CCDC [74, 75]. The lattice vectors a_1, a_2, a_3 and the bond lengths i, j and k are given in Å. For definition of the superscripts i, j, k and n see Figure 5.12. Volume is given in Å^3 and the bond angle n in degrees. The geometry and cell optimizations were performed with different plane wave cutoff energies [Ry] and different approximations. The results of the geometry and cell optimizations are given as relative error, defined in equation (4.5).

Cutoff	Volume	a_1	a_2	a_3	CuO^i	CuO^j	CuO^k	$OCuO^n$
Experimental data								
	790.4	14.195	8.955	6.218	2.409	1.974	1.9277	87.96
DZVP basis								
510	0.111	0.025	0.024	0.058	0.013	0.090	0.025	0.022
610	0.133	0.030	0.030	0.067	0.017	0.115	0.018	0.020
690	0.146	0.036	0.030	0.074	0.013	0.129	0.025	0.023
with D3 correction								
510	0.052	0.017	0.006	0.028	0.016	0.027	0.021	0.009
610	0.053	0.024	0.000	0.028	0.017	0.044	0.020	0.002
690	0.045	0.012	0.011	0.022	0.018	0.045	0.020	0.001
DZVP SR basis with D3 correction								
510	0.046	0.017	0.006	0.023	0.023	0.015	0.020	0.011
and with repeated cell in a_3 direction								
510	0.027	0.013	0.017	0.030	-0.004	0.016	0.029	-0.014
Mixed TZVP SR and TZVP basis with D3 correction								
510	0.053	0.017	0.005	0.029	0.016	0.024	0.020	0.008
DZVP SR and with PBE0 functional								
510	0.037	0.006	0.002	0.028	0.016	0.007	0.019	0.013

More importantly, one can observe that the calculations done without the Grimme D3 correction performs inadequately. For instance the volume and the CuO^j bond has a percent error of over 10%. The inclusion of D3 correction however improves the results so that max percent error is no larger than 5.4%. Moreover, the results does not appear to deviate significantly with the increase in plane wave cutoff, i.e. the cutoff is well behaved. Increasing the basis set size to TZVP does not show to give any increased accuracy. Note that the basis set is a mixture of TZVP SR for Cu atoms and TZVP for carbon, oxygen

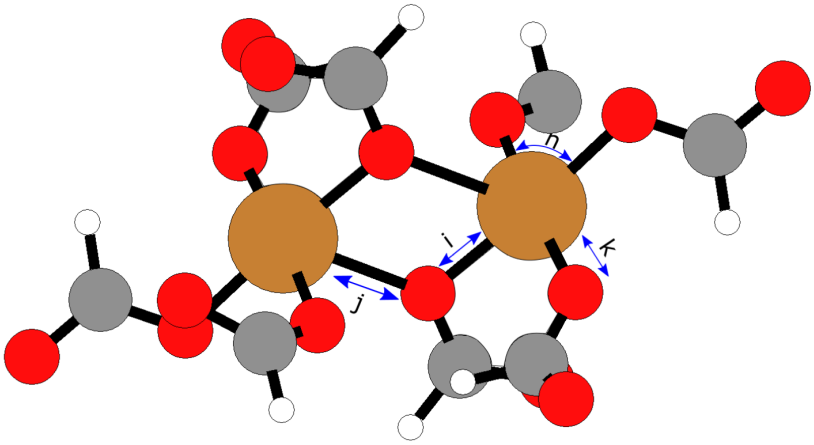

Figure 5.12: The different bond lengths i, j, k and bond angle n computed in this work.

and hydrogen atoms. This was done since only SR version of the basis set is available. Increasing the complexity of the XC functional, namely the hybrid functional PBE0 with the ADMM method, showed signs of giving more accurate lattice parameters. More tests should be made to say something definite, but it is clear that the the PBE0 functional accounts for the dispersion forces better than the PBE functional, and there is no need for D3 correction. Next step to possibly to increase the accuracy would be to use a TZVP basis set.

To conclude, the approximation done with plane wave cutoff of 510 Ry, DZVP basis set, single unit cell with periodic boundary conditions and D3 correction gives satisfactory results at a low computational cost and have been applied as default for this system. In addition the relaxed geometry and cell parameters are used as default geometry.

Vibrational analysis

The calculated IR absorption spectra are shown in Figure 5.13.

Table 5.12: Calculated vibrational frequencies (cm^{-1}) compared with reported literature values.

Calc.	Ref. [76]	Ref. [77]	Vibrational mode description
3045	2910	2758, 1916, 2998	v_1(C-H stretch)
1540	1568	1547, 1596, 1608	v_2(C-O antisym. stretch)
1373	1368	1381, 1401	v_3(C-H in plane bend)
1373	1380	1355, 1366	v_3(C-O sym. stretch)
1007	-	1046, 1065	v_5(out of plane C-H bend
856	833	809, 826	v_4(O-C-O sym. bend)
430	420	302-433	v_5(Cu-O formate stretch)
225	-	153-253	v_6(formate lattice)

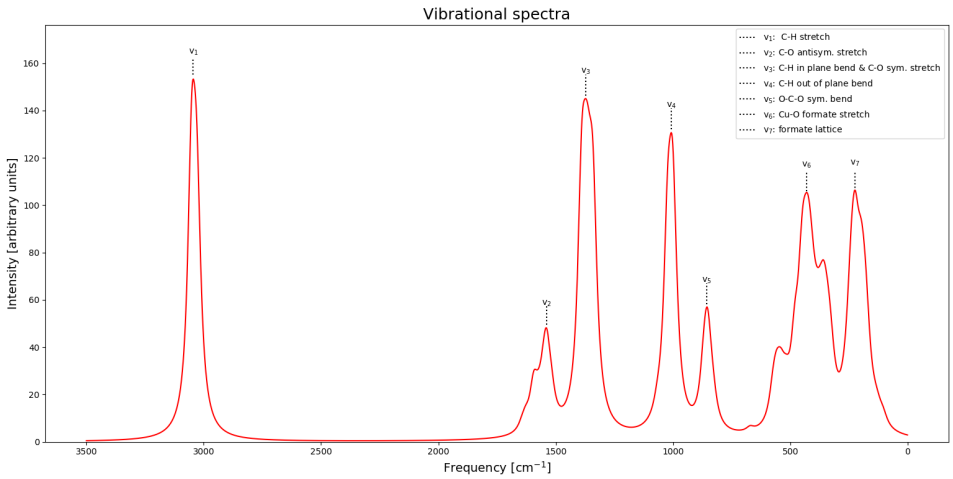

Figure 5.13: Calculated IR absorption spectra with identified vibrational modes ν_1, ν_2...

The vibrational modes have been identified by dynamical visualization of the different vibrational frequencies. In table 5.12 the calculated vibrational modes are compared with references [76, 77]. The estimated values agrees within 5 % error with the first reference. For the second reference several values were reported for each vibrational mode, hence it should be compared rather with the calculated spectra since estimated values in the table 5.12 are peak-values. Overall there seems to be a good agreement with experimental values.

Stretch of the Cu-O formate

Each of the Cu atoms was coordinated by 4 oxygen in a plane at $\sim$1.95 Å and by a fifth oxygen atom at Cu-O^j = 2.41 Å along a line which makes an angle of 71 degrees with this plane. The strength of this prolonged bond is interesting to measure and to see if there is any charge transfer occurring when going from a 5 coordinated structure to a 4 coordinated. The fifth oxygen was translated radially accordingly to Figure 5.14, whereupon the geometry was relaxed. To prohibit the oxygen to relax back to its equilibrium position it was fixed in space.

The result of the stretch is plotted in Figure 5.14. In this method only the oxygen atom is translated, but one can observe from Figure 5.14 (b) that it equivalates to the stretch of the formate. Moreover, the relaxed geometry depicted here is the case when the bond length Cu-O^j=3.37 Å. Already here one would suspect that the bond is broken, and a question arise if there is any different charge distribution.

DDEC6 Population analysis

The results of the DDEC6 bond and charge analysis done on the unperturbed crystal structure and on the stretched Cu-O^j formate bond is presented in table 5.13. The average Cu-O^j bond order for the 8 Cu atoms in the unit cell decreases barely. However, for two

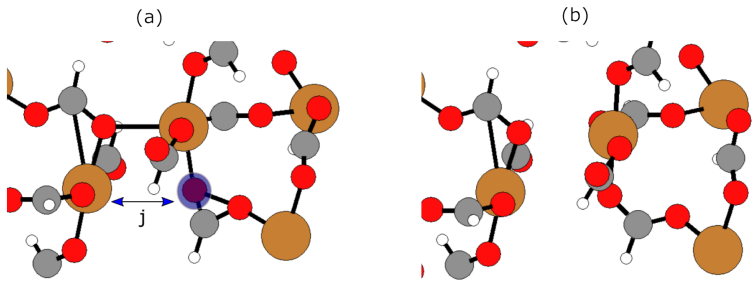

Figure 5.14: The oxygen atom marked in blue shade in part (a) is moved consecutively at longer and longer bond lengths Cu-O^j. The geometry is then relaxed and the resulting relaxation of part (a) is depicted in part (b). The bond length Cu-O^j in part (b) is 3.37 Å

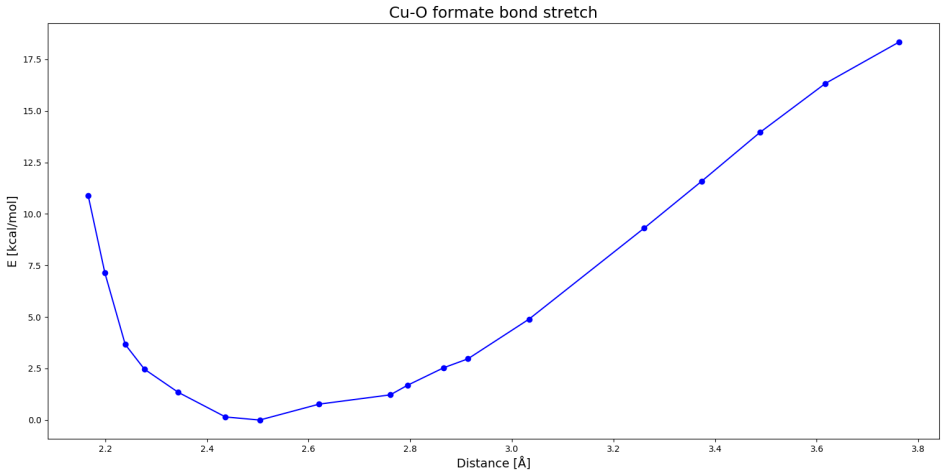

Figure 5.15: The energy difference between the ground state geometry and the geometry resulting from the oxygen stretch is plotted against the resulting Cu-O^j bond length.

of the Cu atoms, a bond order of 0.07 and 0.08 was observed. That is, in terms of covalent bonding the bond is on the verge of being broken, and thus one may say the two of the eight Cu complexes are 4 coordinated. But taking the charges into consideration, it is not observed any noticeable change in charges, meaning the Cu complexes are still in the Cu(II) state. So one should keep in mind that the bond is still very much in place, just with a stronger ionic character.

Decomposition Mechanism

The Cu(I) intermediate of the Cu[HCOO]$_2$ crystal structure has been proven to exist [6]. The structure of the Cu(I) intermediate in Figure 1.1 has not yet been exhaustively verified. With the assumption it is correct, then the reduction from Cu(II) $\rightarrow$ Cu(I) involves a

Table 5.13: Results from the DDEC6 charge and bond order analysis performed on the ground state crystal structure and on the geometry with stretched Cu-O^j formate bond at 3.76 Å. Table (a) contains the average bond order. Superscript with i denotes oxygen atoms constituting a square plane, while superscript j denotes axial bond. Table (b) contains the sum of bond orders and charges.

(a)

Bond	Bond order
Ground state	
Cu-O^i	0.42
Cu-O^j	0.14
C-O	1.58
C-H	0.79
Stretched geometry	
Cu-O^i	0.42
Cu-O^j	0.11
C-O	1.58
C-H	0.79

(b)

Element	Sum of bond orders	Charge
Ground state		
Cu	2.00	1.03
O	2.43	-0.54
C	4.12	0.51
H	1.00	0.05
Stretched geometry		
Cu	2.00	1.02
O	2.43	-0.54
C	4.13	0.51
H	1.00	0.05

big structural rearrangement, where the formate bridging bonds are broken and Cu_2 dimer complexes are formed. Moreover, $Cu[HCOO]_2$ has higher reduction temperature than the other Cu MOD inks. As previously mentioned Marcal et al. connected the reduction temperature to structural differences between the Cu(II) and Cu(I) complexes and the stability of the intermediate [3]. With that in mind, it is understandable that the large structural rearrangement necessary to form the Cu(I) intermediate involves a high reduction temperature.

In the Cu(II) crystal there is 2.5 formates per Cu center, while in the deduced Cu(I) structure there is 1 formate per Cu center. So in order for the structural rearrangement to be achievable under thermal curing, some of the formates have to evaporate away. The results of the bond stretching calculations in gas phase and for the crystal have shown that simply stretching the bond until breakage does not yield the required charge transfer, even though the coordination number changes. The formate really likes its excess electron. therefore, the evaporation of formate involves a thermal decomposition to gaseous products, mainly CO_2 [3]. A suggestion for the thermal decomposition of the formate anions in the crystal structure is the protonation of the formates, i.e. formic acid. Formic acid has been shown to thermally decompose in the gas phase to mainly CO_2 and H_2 at elevated temperatures [78]. In addition it can be speculated that the protonation of the formate reduces the bonding strength to the Cu centers, and thus will more readily be released and decompose. To test this, one of the formate's hydrogen was moved $a = 1.89$ Å to protonate one of the formates. Part (a) of Figure 5.16 shows this hydrogen with a pink shade.

It was then performed a geometry optimization and the relaxed structure is shown in part (b) of the Figure. The energy difference between the relaxed structure and the ground state crystal structure is just $E_{\mathrm{GS}} - E_{\mathrm{prot}} = 34.97$ kcal/mol. The DDEC6 charge and bond order analysis is given in table 5.14.

The DDEC6 charges indicate that a charge transfer has occurred to the Cu(43), from

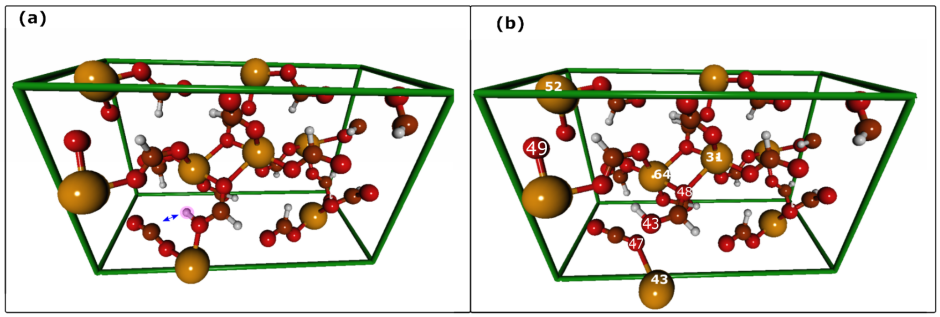

Figure 5.16: Part (a), the pink hydrogen is moved to the depicted position. The structure is then relaxed and yields the structure in part (b). This simulates the result of a proton tunneling effect. Some atoms are given numbers to easier to keep track of different atoms.

Table 5.14: The DDEC6 charges on selected Cu and the average value for the Cu in the unit cell is shown in part (a). In part (b) all bond orders above 0.07 are shown for selected Cu atoms and the average for the Cu in the unit cell. Superscript a denotes the bond Cu(43)-O(47), b the bond Cu(52)-O(49) and c the bond Cu(52)-O(48).

(a)

Element	Charge
Cu(43)	0.50
Cu(52)	0.65
Cu(64)	0.88
Cu_{avg}	0.89

(b)

Cu	Cu-O
Cu(43)	0.07 0.14^a, 0.14, 0.65, 0.65
Cu(52)	0.07^b, 0.25, 0.38, 0.48, 0.54
Cu(64)	0.17, 0.34^c, 0.40, 0.44, 0.44
Cu_{avg}	0.36

the formation of CO_2 and protonation of one formate. The bond orders also reveals that the oxygen are not that well bonded to the Cu atoms anymore, in terms of covalent bonding, especially for Cu(43) and Cu(52). The Cu(64) is now coordinated to the formic acid, HCOOH, which should be a weaker bond. The inertness of CO_2 molecule can be seen from the bond orders as well. The bonds Cu(43)-O(47) and Cu(52)-Cu(47) has only a bond order of 0.14 and 0.07 respectively.

This simulation can be seen as the result of a proton tunneling effect. Furthermore, it shows that one such event makes several of the coordination bonds weaker. The inertness of CO_2 allows the latter to evaporate freely away, while the formate acid can further decompose to CO_2 and H_2 gas. Yet to be determined is the energy barrier to see if this is in fact a reliably mechanism for the decomposition of Cu(II) complex at elevated temperatures.

Band Gap

The projected density of states (PDOS) was calculated to determine the band gap of the $Cu[HCOO]_2$ crystal structure. The band gap is defined as the energy difference between the highest occupied molecular orbital (HOMO) and lowest unoccupied molecular orbital

(LUMO). The density of states projected per atom was printed out from CP2K and convoluted with a Gaussian function to yield Figure 5.17. Since k-sampling was only done at the gamma point, the calculation was done with multiple unit cells, i.e. a replica in each a_1, a_2 and a_3 direction. This was done in order to achieve a meaningful sampling of the PDOS. The HOMO level is defined as 0 eV. The band gap can then be easily read off as 2.1 eV. Different XC functionals have been tested extensively for their accuracy on the prediction of band gap size [79]. On average the PBE functional underestimated band gaps of about 40 %. The systematic underestimation occurring with PBE can be improved with the inclusion of HF exchange, that is hybrid functionals [80, 79].

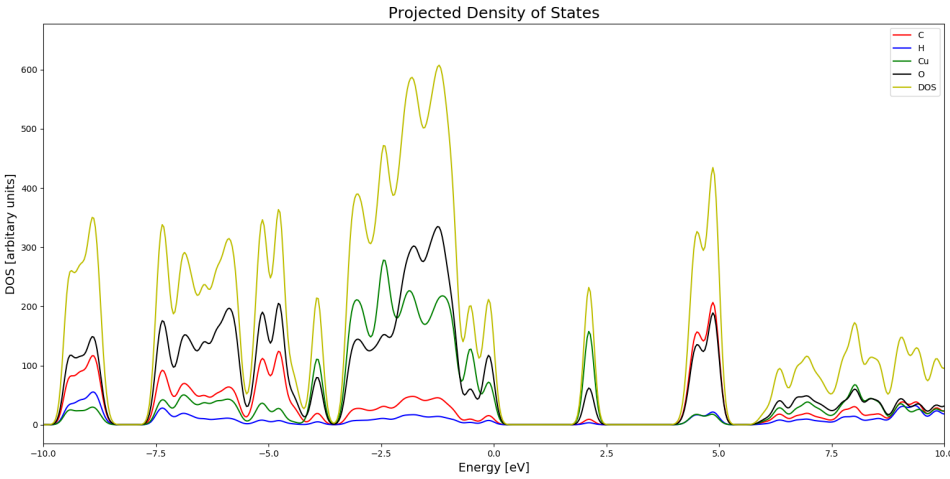

Figure 5.17: The projected density of states (DOS) for the atoms in the $Cu[HCOO]_2$ crystal structure. The HOMO level is defined as 0 eV.

The optimized crystal structure with the hybrid PBE0 functional was used to calculate a new PDOS plot, seen in Figure 5.18. Here it is noticeable that the k-sampling is too coarse, due to only a single unit cell was used. Increasing the computational cell size with more unit cells, would however, be very demanding with the PBE0 functional. The band gap with the PBE0 functional is 5.8 eV. No earlier determination of the band gap has been found in the literature.

5.3.2 Copper Ethylenediamine Formate

The crystal structure of $Cu(en)_2[HCOO]_2$ is shown in Figure 5.19. The unit cell has a monoclinic symmetry and the crystal structure contains discrete units of $Cu(en)_2[HCOO]_2$ molecules, that is no bridging network as for the $Cu[HCOO]_2$ crystal structure.

The result of the geometry and cell optimization can be found in table 5.15. It was mentioned earlier that the gamma point sampling may not be sufficient for small unit cells. The lattice vector for this crystal structure in a_2 direction is quite small, and from the table 5.15 one can see that the calculation fails quite miserably, with errors up to 20 % compared to experimental values. Replicating the unit cell once in the a_2 direction (denoted MU(1

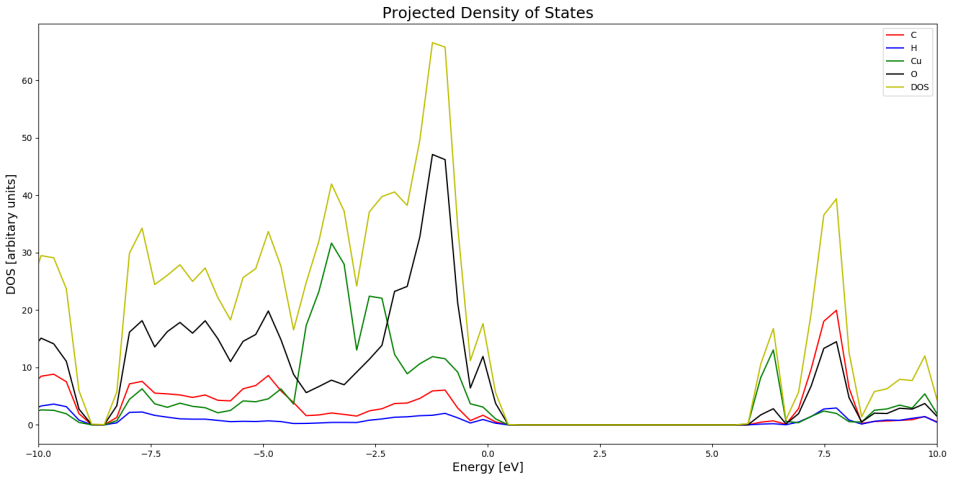

Figure 5.18: The projected density of states (DOS) for the atoms in the $Cu[HCOO]_2$ crystal structure calculated with the PBE0 functional. The HOMO level is defined as 0 eV.

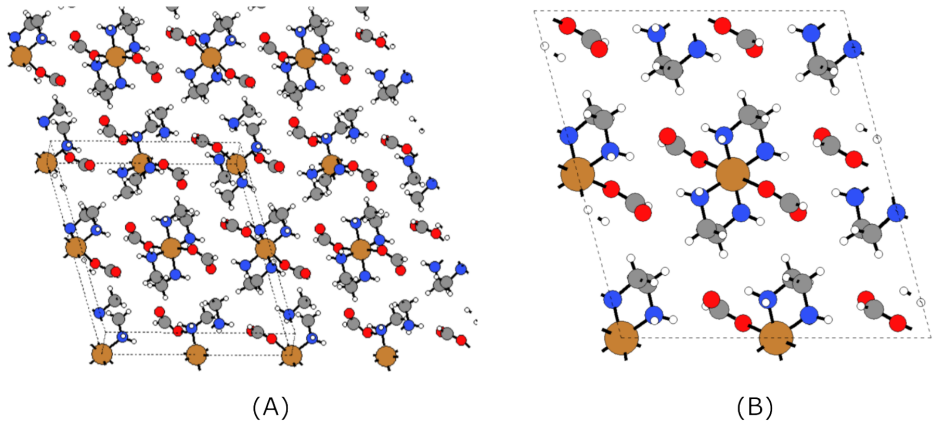

Figure 5.19: The crystal structure of $Cu(en)_2[HCCO]_2$. Part (A) shows unit cell repeated in a_1 and a_3 direction. The sole unit cell (B) is depicted in the a_1-a_3 plane.

2 1) in Figure), solves the problem partly. Without the grimme D3 correction the errors are still not yet acceptable, as the CuO bond length has errors of about 10 %. With the D3 correction the results have all less then 0.05 relative errors. Furthermore, one can observe that increasing the basis set size and including more unit cells does not produce any more accurate results. Increasing the cutoff may have been interesting, but since these calculations require multiple unit cells resulting in already quite high computational cost, and since the errors are within acceptable range, there is no need.

Table 5.15: The experimental data is taken from CCDC [3, 74]. For the experimental data the lattice vectors a_1, a_2, a_3 and the bond lengths Cu-N, Cu-O and Cu-C are given in Å. Volume is given in $Å^3$ and the bond angle N-Cu-N and the angle between lattice vectors a_1 and a_3, i.e. β, in degrees. The geometry and cell optimizations were performed with different different approximations, denoted by (# of multiple unit (MU) cells in direction a_1 a_2 a_3, D3 corrected yes/no, bais set type). The results of the geometry and cell optimizations are given as relative error, defined in equation (4.5).

Volume	a_1	a_2	a_3	β	CuN	CuO	CuC	NCuN
Experimental data								
1100.8	15.318	5.305	14.022	104.968	2.026	2.473	2.838	85.082
MU(1 1 1), D3 Yes, DZVP								
0.011	0.145	-0.200	0.173	0.093	0.030	0.504	0.021	-0.008
MU(1 2 1), D3 No, SR DZVP								
0.158	0.097	0.065	0.004	0.023	0.019	0.104	0.010	-0.003
MU(1 2 1), D3 Yes, SR DZVP								
0.000	0.011	-0.001	-0.002	0.015	0.019	0.022	0.005	-0.003
MU(1 2 1), D3 Yes, SR TZVP								
0.013	0.010	0.005	0.005	0.013	0.014	0.029	0.004	-0.002
MU(2 2 2), D3 Yes, SR DZVP								
0.000	0.011	-0.001	-0.042	0.014	0.016	0.026	0.005	-0.002

Stretch of the Cu-O formate bond

The oxygen atom was perturbed and fixed in space in the same manner as for the Cu-$[HCOO]_2$ crystal. The result of the the calculation is shown in Figure 5.20. The energy required to stretch the formate for this crystal is noticeable lower, around half the energy. Moreover, the reduction of the Cu(II) state to Cu(I) involves only one formate evaporation per Cu center. And from this perspective one can understand why the reduction temperature is lower than for the $Cu[HCOO]_2$ crystal. The DDEC6 charge on the Cu subjected to the stretched formate bond was calculated to be 0.74 and the average Cu charge value was 0.75. This is consistent with Cu to be in the Cu(II) state.

5.3.3 Copper Pyridine Formate

The ground state crystal structure of $Cu(pyr)_2[HCOO]_2$ depicted in Figure 5.21 shows that the Cu atoms are connected in a bridge network of formates. The Cu center is coordinated by three formates and two pyridine ligands forming a tetragonal pyramid structure.

Table 5.16 shows the result of the geometry and cell optimization. The simulations were performed with different cutoff energies, which did not show any clear difference. The simulations that included the Grimme's D3 dispersion correction yielded in fact worse results than without. It seems like it overcompensates and the structure becomes compressed in the a_3 direction. Without the correction the relative errors are still somewhat high but still better than with the dispersion correction.

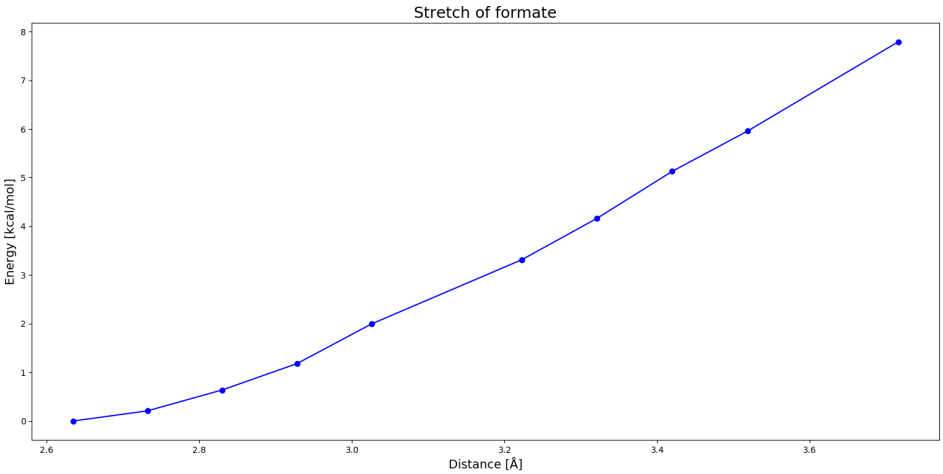

Figure 5.20: The energy required to stretch the Cu-O formate to certain distances.

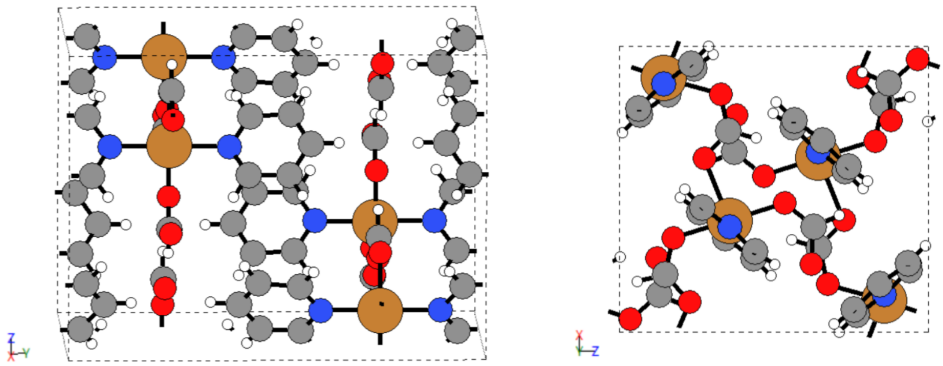

Figure 5.21: The crystal structure of $Cu(pyr)_2[HCCO]_2$ is depicted in two different perspectives.

Vibrational analysis

For the vibrational analysis a plane wave cutoff of 480 Ry and without dispersion correction have been used, as this setup was the best with respect to accuracy and computational cost. The IR vibrational spectra calculated is presented in Figure 5.22. Since the crystal contains different kind of bonds and elements, there are frequency intervals where different vibrational modes occur. For instance the peak marked as c in the plot is associated with stretch of the formate's O and pyridine's C.

Table 5.16: The experimental data is taken from CCDC [74, 3]. For the experimental data the lattice vectors a_1, a_2, a_3 and the bond lengths Cu-N, Cu-O and Cu-C are given in Å, volume (Å^3) and the bond angle O-Cu-N in degrees. The Cu-O bond is with the oxygen constituting the coordinated square plane. The geometry and cell optimizations were performed with different different energy plane wave cutoffs (Ry) and test with and without the D3 dispersion correction. The results of the geometry and cell optimizations are given as relative error, defined in equation (4.5).

Cutoff	Volume	a_1	a_2	a_3	CN	CuN	CuO	OCuN
				Experimental data				
	1408.36	9.627	14.067	10.400	1.346	2.021	1.951	91.521
				Without D3 correction				
480	0.127	0.055	0.067	0.001	0.003	0.008	0.030	0.002
640	0.123	0.042	0.064	0.013	0.003	0.009	0.031	0.002
				With D3 correction				
480	-0.111	0.049	0.073	-0.211	0.003	0.003	0.029	0.001
540	-0.110	0.050	0.074	-0.210	0.003	-0.001	0.028	0.010

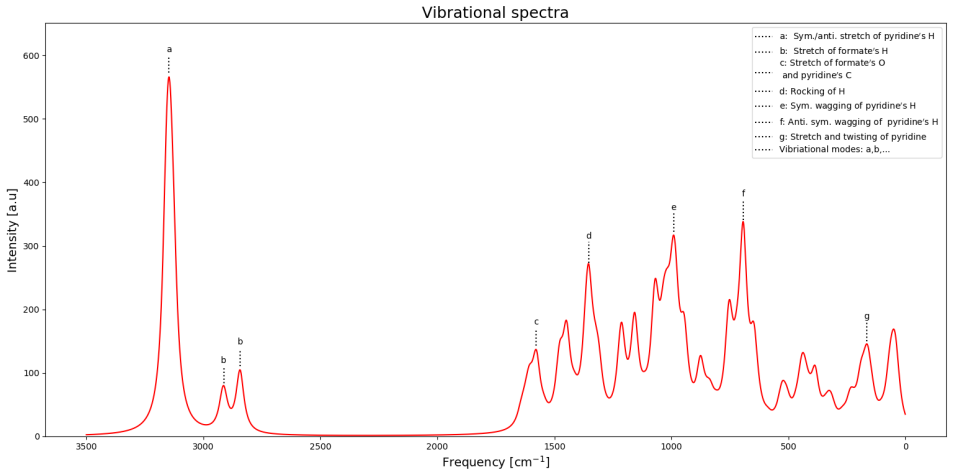

Figure 5.22: Calculated IR spectra of the $Cu(pyr)_2[HCOO]_2$ crystal structure. The identified vibrational modes can be found in the legend.

5.4 Molecular Dynamics

MD simulations were done on the crystal structure $Cu[HCOO]_2$, with constant temperature of 300, 400 and 500 Kelvin. Before the production run, the geometry was equilibrated at each of these temperature. This is to ensure that it does not start in an unlikely state. To do this a temperature tolerance of 50 K was used for 2000 fs. This allows the temperature to vary with 50 K before a velocity rescaling occur. In this system hydrogen has the highest vibrational frequencies of around, so to sample the motion with good enough accuracy time steps of 0.5 fs was used. The simulations were run for 8.5 ps and the resulting radial

distribution function g(r) from the MD run is presented in Figure5.23. It shows how the density of oxygen varies with respect to the Cu atom. The first peak corresponds to the oxygen coordinated in the distorted square, while the next peak is the coordinated axial oxygen. The first peak for the 300K run, is located at 1.97 Å. This is in accordance to the value calculated from static geometry optimization, as the peak corresponds to where the oxygen is found most likely. The second peak corresponding to the the axial oxygen is very broad. This shows how loosely bound this formate is, as it moves quite a lot. With increasing temperature one can observe the oxygen are distributed more unevenly, i.e. broader peaks, as one would expect. The center of the peaks for all three temperatures are approximately the same, thus no coordination change is observed. The sampling is done over a very small time frame, 8.5 ps, so for a reaction to occur is not probable. In addition this simulates a closed system, where all the Cu are interconnected through the bridging of formates. Hence it is not possible for the formates to evaporate, and therefore making it impossible to form the Cu(I) intermediate. Thus the MD simulations on this system is not interesting with regards to the reduction process.

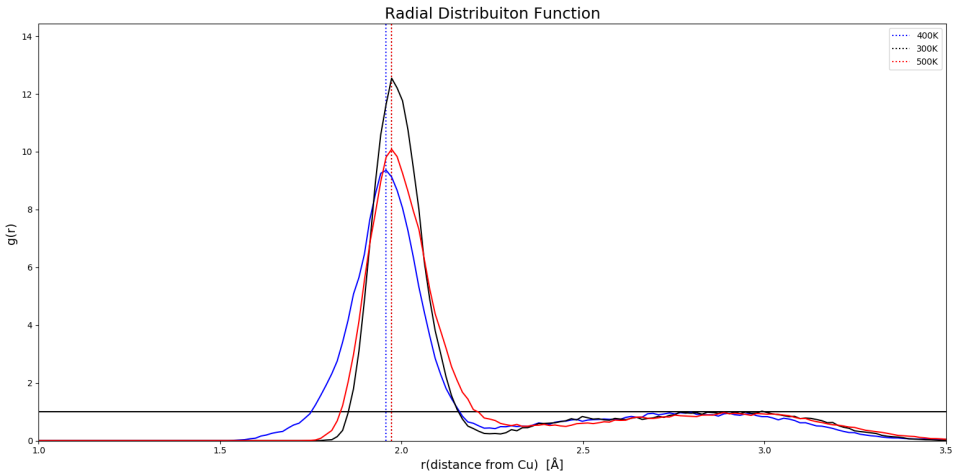

Figure 5.23: The radial distribution function of oxygen with respect to Cu, average taken over 8.75 ps. The peak corresponding to the square coordinated oxygen is denoted by striped lines. The 300K and 500K peak coincide.

Chapter 6

Conclusion

DFT and MD simulations have been used to investigate different types of Cu formate complexes in the gas phase and as crystalline solid. The complexes considered as crystalline solids were $Cu[HCOO]_2$, $Cu(en)_2[HCCO]_2$ and $Cu(pyr)_2[HCOO]_2$. The calculations showed that the PBE functional adjusted with the Grimme D3 dispersion correction was crucial in order for the geometry and cell parameters to relax to the experimental data within acceptable values. Increasing the basis set size to TZVP basis did not further improve the results. In addition, the hybrid functional PBE0 was tested on the $Cu[HCOO]_2$ crystal without the dispersion correction, and gave similar results as the D3-PBE functional. For the $Cu_2(pyr)[HCOO]_2$ crystal the D3 correction overcompensated the dispersion interactions, and proved worse than without. One of the formates were stretched in the crystals, $Cu[HCOO]_2$ and $Cu(en)_2[HCCO]_2$, to see how strong the bonds were, as this might be an important part of the thermal reduction pathway. The formate in the crystal $Cu(en)_2[HCOO]_2$ was found to be weaker than for $Cu[HCOO]_2$ which coincides with $Cu(en)_2[HCOO]_2$ having a lower reduction temperature. Furthermore, a decomposition mechanism for the $Cu[HCOO]_2$ crystal was suggested. This mechanism involves the proton tunneling between two formates, which could start the reaction of further decomposing the crystal at elevated temperatures. More investigation should be made.

The calculated IR spectra for the two crystal structures $Cu[HCOO]_2$ and $Cu(pyr)_2[HCOO]_2$ are presented. The vibrational spectrum for $Cu(pyr)_2[HCOO]_2$ have not been previously reported, but for the other crystals the spectra is agrees well with literature especially for $Cu[HCOO]_2$. In addition the band gap for the $Cu[HCOO]_2$ crystal is reported with the PBE and PBE0 functional, with values 2.1 eV and 5.8 eV.

The crystal Cu(II) intermediate $Cu_2(pyr)[HCOO]_2$ and the crystal $Cu(en)_2[HCOO]_2$ consists of discrete units of the respective complexes. These complexes were therefore simulated in the gas phase to learn more about the formate bond strength, and the reduction to the intermediate $Cu_2(pyr)[HCOO]$ and $Cu(en)_2[HCOO]$. The calculations does not have good enough resolution to be able to determine the structural complex, $Cu(en)_2[HCOO]$, which has not yet been verified experimentally either. The $Cu_2(pyr)[HCOO]$ intermediate could possibly have anti parallel spin or parallel spin on the Cu centers, implying either a

singlet or triplet state.

The bond strength of the Cu-formate was also probed in the gas phase, as the reduction of these complexes involve the decomposition of one formate per Cu center. It was found that the strength of the Cu-formate bonds in the three Cu complexes tested was ordered as $Cu[HCOO]_2$, $Cu(en)_2[HCOO]_2$ $Cu_2(pyr)[HCOO]_2$, from strongest to weakest. This corresponds to the relative order of their reduction temperature in the crystal phase.

Bibliography

[1] Bong Kyun Park, Dongjo Kim, Sunho Jeong, Jooho Moon, and Jang Sub Kim. Direct writing of copper conductive patterns by ink-jet printing. *Thin Solid Films*, 515(19):7706 – 7711, 2007. Proceedings of Symposium I on Thin Films for Large Area Electronics EMRS 2007 Conference.

[2] Alexander Kamyshny, Joachim Steinke, and Shlomo Magdassi. Metal-based inkjet inks for printed electronics. *The Open Applied Physics Journal*, 411:19–36, 03 2011.

[3] Wouter Marchal, Alessandro Longo, Valérie Briois, Kristof Van Hecke, Ken Elen, Marlies K. Van Bael, and An Hardy. Understanding the importance of cu(i) intermediates in self-reducing molecular inks for flexible electronics. *Inorganic Chemistry*, 57(24):15205–15215, 2018.

[4] Zheng Cui. *Printed Electronics : Materials, Technologies and Applications*. John Wiley Sons, Incorporated, 2016, 2016.

[5] Michael Grouchko, Alexander Kamyshny, Cristina Florentina Mihailescu, Dan Florin Anghel, and Shlomo Magdassi. Conductive inks with a "built-in" mechanism that enables sintering at room temperature. *ACS Nano*, 5(4):3354–3359, 2011. PMID: 21438563.

[6] Yousef Farraj, Michael Grouchko, and Shlomo Magdassi. Self-reduction of a copper complex mod ink for inkjet printing conductive patterns on plastics. *Chem. Commun.*, 51:1587–1590, 2015.

[7] Yun-Hyuk Choi and Seong-Hyeon Hong. Effect of the amine concentration on phase evolution and densification in printed films using cu(ii) complex ink. *Langmuir*, 31(29):8101–8110, 2015. PMID: 26151862.

[8] Chantal Paquet, Thomas Lacelle, Xiangyang Liu, Bhavana Deore, Arnold J. Kell, Sylvie Lafrenière, and Patrick R. L. Malenfant. The role of amine ligands in governing film morphology and electrical properties of copper films derived from copper formate-based molecular inks. *Nanoscale*, 10:6911–6921, 2018.

[9] R. O. Jones. Density functional theory: Its origins, rise to prominence, and future. *Rev. Mod. Phys.*, 87:897–923, Aug 2015.

[10] S. Zumdahl. *Chemical principles*. CENGAGE Learning Custom Publishing, 6th edition, 2009.

[11] Javad Hashemi William Smith. *Foundations of Materials Science and Engineering*. McGraw Hill 5th edition, 2010.

[12] *Low-Temperature Physics*. Springer Berlin Heidelberg, Berlin, Heidelberg, 2005.

[13] David B. Rorabacher. Electron transfer by copper centers. *Chemical Reviews*, 104(2):651–698, 2004. PMID: 14871138.

[14] Charles Kittel. *Introduction to Solid States Physics*. Wiley 8th edition, 2012.

[15] F. Jensen. *Introduction to computational chemistry*. WILEY, 2. edition, 2007.

[16] Robert G. Parr and Y. Weitao. *Density Functional Theory of Atoms and Molecules*. Oxford university press, 1987.

[17] P.C Hemmer. *Kvantemekanikk*. Fagbokforlaget 5th edition, 2005.

[18] N. Handy. The importance of colle–salvetti for computational density functional theory. 2009.

[19] P. Hohenberg and W. Kohn. Inhomogeneuous electron gas. 1964.

[20] M. Levy. Universal variational functionals of electron densities, first-order density matrices, and natural spin-orbitals and solution of the v-representability problem. 1979.

[21] W. Kohn and L. J. Sham. Self-consistent equations including exchange and correlation effects. *Phys. Rev.*, 140:A1133–A1138, Nov 1965.

[22] Jianmin Tao Viktor N. Staroverov Gustavo E. Scuseria et al. John P. Perdew, Adrienn Ruzsinszky. Prescription for the design and selection of density functional approximations: More constraint satisfaction with fewer fits.

[23] S. H. Vosko, L. Wilk, and M. Nusair. Accurate spin-dependent electron liquid correlation energies for local spin density calculations: a critical analysis. *Canadian Journal of Physics*, 58(8):1200–1211, 1980.

[24] Stefan Kurth, John P. Perdew, and Peter Blaha. Molecular and solid-state tests of density functional approximations: Lsd, ggas, and meta-ggas. *International Journal of Quantum Chemistry*, 75(4-5):889–909, 1 1999.

[25] O. Gunnarsson, M. Jonson, and B. I. Lundqvist. Descriptions of exchange and correlation effects in inhomogeneous electron systems. *Phys. Rev. B*, 20:3136–3164, Oct 1979.

[26] Kieron Burke, John P. Perdew, and Matthias Ernzerhof. Why semilocal functionals work: Accuracy of the on-top pair density and importance of system averaging. *The Journal of Chemical Physics*, 109(10):3760–3771, 1998.

[27] G. F. Giuliani and G. Vignale. *Quantum Theory of the Electron Liquid*. New York: Cambridge University Press, 2005.

[28] John P. Perdew, Kieron Burke, and Matthias Ernzerhof. Generalized gradient approximation made simple. *Phys. Rev. Lett.*, 77:3865–3868, Oct 1996.

[29] A. D. Becke. Density-functional exchange-energy approximation with correct asymptotic behavior. *Phys. Rev. A*, 38:3098–3100, Sep 1988.

[30] Chengteh Lee, Weitao Yang, and Robert G. Parr. Development of the colle-salvetti correlation-energy formula into a functional of the electron density. *Phys. Rev. B*, 37:785–789, Jan 1988.

[31] Xin Xu and William A. Goddard. The x3lyp extended density functional for accurate descriptions of nonbond interactions, spin states, and thermochemical properties. *Proceedings of the National Academy of Sciences*, 101(9):2673–2677, 2004.

[32] Axel D. Becke. A new mixing of hartree–fock and local density-functional theories. *The Journal of Chemical Physics*, 98(2):1372–1377, 1993.

[33] Carlo Adamo and Vincenzo Barone. Toward reliable density functional methods without adjustable parameters: The pbe0 model. *The Journal of Chemical Physics*, 110(13):6158–6170, 1999.

[34] Christoph R. Jacob and Markus Reiher. Spin in density-functional theory. *International Journal of Quantum Chemistry*, 112(23):3661–3684, Aug 2012.

[35] Eberhard Engel and Reiner M. Dreizler. *Relativistic Density Functional Theory*. Springer Berlin Heidelberg, Berlin, Heidelberg, 2011.

[36] TITLE = Ab Initio Molecular Dynamics Basic Theory and Advanced Methods PUBLISHER = Cambridge university press YEAR = 2009 Pages = Dominik Marx, Jürg Hutter.

[37] Richard M. Martin. *Electronic Structure : Basic Theory and Practical Methods.*, volume 1st pbk. ed. with corrections. Cambridge University Press, 2008.

[38] Friedhelm Bechstedt. *Many-Body Approach to Electronic Excitations: Concepts and Applications*. Springer Berlin Heidelberg, Berlin, Heidelberg, 2015.

[39] *Density Functional Theory: A Practical Introduction*, chapter 3, pages 49–81. John Wiley Sons, Ltd, 2009.

[40] The cp2k developers group. cp2k is freely available from http://www.cp2k.org/ (accessed , 2019).

[41] J VandeVondele, M Krack, F Mohamed, M Parrinello, T Chassaing, and J Hutter. Quickstep: Fast and accurate density functional calculations using a mixed gaussian and plane waves approach. *Computer Physics Communications*, 167(2):103–128, 2005.

[42] Gerald Lippert, Jürg Hutter, and Michele Parrinello. The gaussian and augmented-plane-wave density functional method for ab initio molecular dynamics simulations. *Theoretical Chemistry Accounts*, 103(2):124–140, Dec 1999.

[43] By GERALD LIPPERT, JURG HUTTER, and MICHELE PARRINELLO. A hybrid gaussian and plane wave density functional scheme. *Molecular Physics*, 92(3):477–488, 1997.

[44] Joost VandeVondele and Jürg Hutter. An efficient orbital transformation method for electronic structure calculations. *The Journal of Chemical Physics*, 118(10):4365–4369, 2003.

[45] Manuel Guidon, Jürg Hutter, and Joost VandeVondele. Auxiliary density matrix methods for hartreefock exchange calculations. *Journal of Chemical Theory and Computation*, 6(8):2348–2364, 2010. PMID: 26613491.

[46] S. Goedecker, M. Teter, and J. Hutter. Separable dual-space gaussian pseudopotentials. *Phys. Rev. B*, 54:1703–1710, Jul 1996.

[47] C. Hartwigsen, S. Goedecker, and J. Hutter. Relativistic separable dual-space gaussian pseudopotentials from h to rn. *Phys. Rev. B*, 58:3641–3662, Aug 1998.

[48] M. Krack. Pseudopotentials for h to kr optimized for gradient-corrected exchange-correlation functionals. *Theoretical Chemistry Accounts*, 114(1):145–152, Sep 2005.

[49] Joost VandeVondele and Jürg Hutter. Gaussian basis sets for accurate calculations on molecular systems in gas and condensed phases. *The Journal of Chemical Physics*, 127(11):114105, 2007.

[50] David Yarkony. *Modern Electronic Structure Theory (In 2 Parts) - Part 1*. Number v. 2 in Advanced Series in Physical Chemistry. World Scientific, 1995.

[51] R. Fletcher. *Newton-Like Methods*. John Wiley Sons, Ltd, 2013.

[52] D. F. Shanno. Conditioning of quasi-newton methods for function minimization. *Mathematics of Computation*, 24(111):647–656, 1970.

[53] R. F. Bader. *Atoms in Molecules: A Quantum Theory*. Oxford University Press, 1990.

[54] Graeme Henkelman, Andri Arnaldsson, and Hannes Jónsson. A fast and robust algorithm for bader decomposition of charge density. *Computational Materials Science*, 36(3):354 – 360, 2006.

[55] R. S. Mulliken. Electronic population analysis on lcao–mo molecular wave functions. i. *The Journal of Chemical Physics*, 23(10):1833–1840, 1955.

[56] Thomas A. Manz and Nidia Gabaldon Limas. Ddec6: A method for computing even-tempered net atomic charges in periodic and nonperiodic materials. 2015.

[57] F. L. Hirshfeld. Bonded-atom fragments for describing molecular charge densities. *Theoretica chimica acta*, 44(2):129–138, Jun 1977.

[58] Nidia Gabaldon Limas and Thomas A. Manz. Introducing ddec6 atomic population analysis: part 4. efficient parallel computation of net atomic charges, atomic spin moments, bond orders, and more. *RSC Adv.*, 8:2678–2707, 2018.

[59] T. A. Manz and N. Gabaldon Limas. Chargemol program for performing ddec6 analysis, accessed september 2019.

[60] Thomas A. Manz. Introducing ddec6 atomic population analysis: part 3. comprehensive method to compute bond orders. *RSC Adv.*, 7:45552–45581, 2017.

[61] Roderigh Y. Rohling, Ionut C. Tranca, Emiel J. M. Hensen, and Evgeny A. Pidko. Correlations between density-based bond orders and orbital-based bond energies for chemical bonding analysis. *The Journal of Physical Chemistry C*, 123(5):2843–2854, 2019.

[62] Satish Kumar Iyemperumal and N. Aaron Deskins. Activation of co2 by supported cu clusters. *Phys. Chem. Chem. Phys.*, 19:28788–28807, 2017.

[63] Sándor Kristyán and Péter Pulay. Can (semi)local density functional theory account for the london dispersion forces? *Chemical Physics Letters*, 229(3):175 – 180, 1994.

[64] Stefan Grimme, Jens Antony, Stephan Ehrlich, and Helge Krieg. A consistent and accurate ab initio parametrization of density functional dispersion correction (dft-d) for the 94 elements h-pu. *The Journal of Chemical Physics*, 132(15):154104, 2010.

[65] Jonas Moellmann and Stefan Grimme. Dft-d3 study of some molecular crystals. *The Journal of Physical Chemistry C*, 118(14):7615–7621, 2014.

[66] Editor: Russell D. Johnson III. Nist computational chemistry comparison and benchmark database.

[67] Jeffrey P. Merrick, Damian Moran, and Leo Radom. An evaluation of harmonic vibrational frequency scale factors. *The Journal of Physical Chemistry A*, 111(45):11683–11700, 2007. PMID: 17948971.

[68] Jens O. Andersen. *Introduction to Statistical Mechanics*. Akademica Publishing, 2012.

[69] Jens O. Andersen. *Essentials of Computational Chemistry: Theories and Models*. Christopher J. Cramer, 2004.

[70] Jiří Kolafa. Time-reversible always stable predictor–corrector method for molecular dynamics of polarizable molecules. *Journal of Computational Chemistry*, 25(3):335–342, 2004.

[71] Eric W. Dahl and Nathaniel K. Szymczak. Hydrogen bonds dictate the coordination geometry of copper: Characterization of a square-planar copper(i) complex. *Angewandte Chemie*, 128(9):3153–3157, 2016.

[72] Katsuhiko Takeuchi, Hiro-omi Taguchi, Ippei Tanigawa, Shota Tsujimoto, Tsukasa Matsuo, Hiromasa Tanaka, Kazunari Yoshizawa, and Fumiyuki Ozawa. A square-planar complex of platinum(0). *Angewandte Chemie International Edition*, 55(49):15347–15350, 2016.

[73] W. Marchal, F. Mattelaer, K. Van Hecke, V. Briois, A. Longo, D. Reenaers, K. Elen, C. Detavernier, W. Deferme, M. K. Van Bael, and A. Hardy. Effectiveness of ligand denticity-dependent oxidation protection in copper mod inks. *Langmuir*, 35(49):16101–16110, 2019. PMID: 31697083.

[74] Colin R. Groom, Ian J. Bruno, Matthew P. Lightfoot, and Suzanna C. Ward. The Cambridge Structural Database. *Acta Crystallographica Section B*, 72(2):171–179, Apr 2016.

[75] G. A. Barclay and C. H. L. Kennard. 644. the crystal structure of anhydrous copper(ii) formate. *J. Chem. Soc.*, pages 3289–3294, 1961.

[76] A.M. Heyns. The vibrational spectra of the copper(ii) formates: I. raman spectra of polycrystalline copper(ii) formate tetrahydrate and the light blue modification of anhydrous copper(ii) formate. *Journal of Molecular Structure*, 18(3):471 – 485, 1973.

[77] R.O. Carter, B.D. Poindexter, and W.H. Weber. Vibrational spectra of copper formate tetrahydrate, copper formate dihydrate and three anhydrous forms of copper formate. *Vibrational Spectroscopy*, 2(2):125 – 134, 1991.

[78] W. L. Nelson and C. J. Engelder. The thermal decomposition of formic acid. *The Journal of Physical Chemistry*, 30(4):470–475, 1926.

[79] Pedro Borlido, Thorsten Aull, Ahmad W. Huran, Fabien Tran, Miguel A. L. Marques, and Silvana Botti. Large-scale benchmark of exchange–correlation functionals for the determination of electronic band gaps of solids. *Journal of Chemical Theory and Computation*, 15(9):5069–5079, 2019. PMID: 31306006.

[80] Jason M. Crowley, Jamil Tahir-Kheli, and William A. Goddard. Resolution of the band gap prediction problem for materials design. *The Journal of Physical Chemistry Letters*, 7(7):1198–1203, 2016. PMID: 26944092.

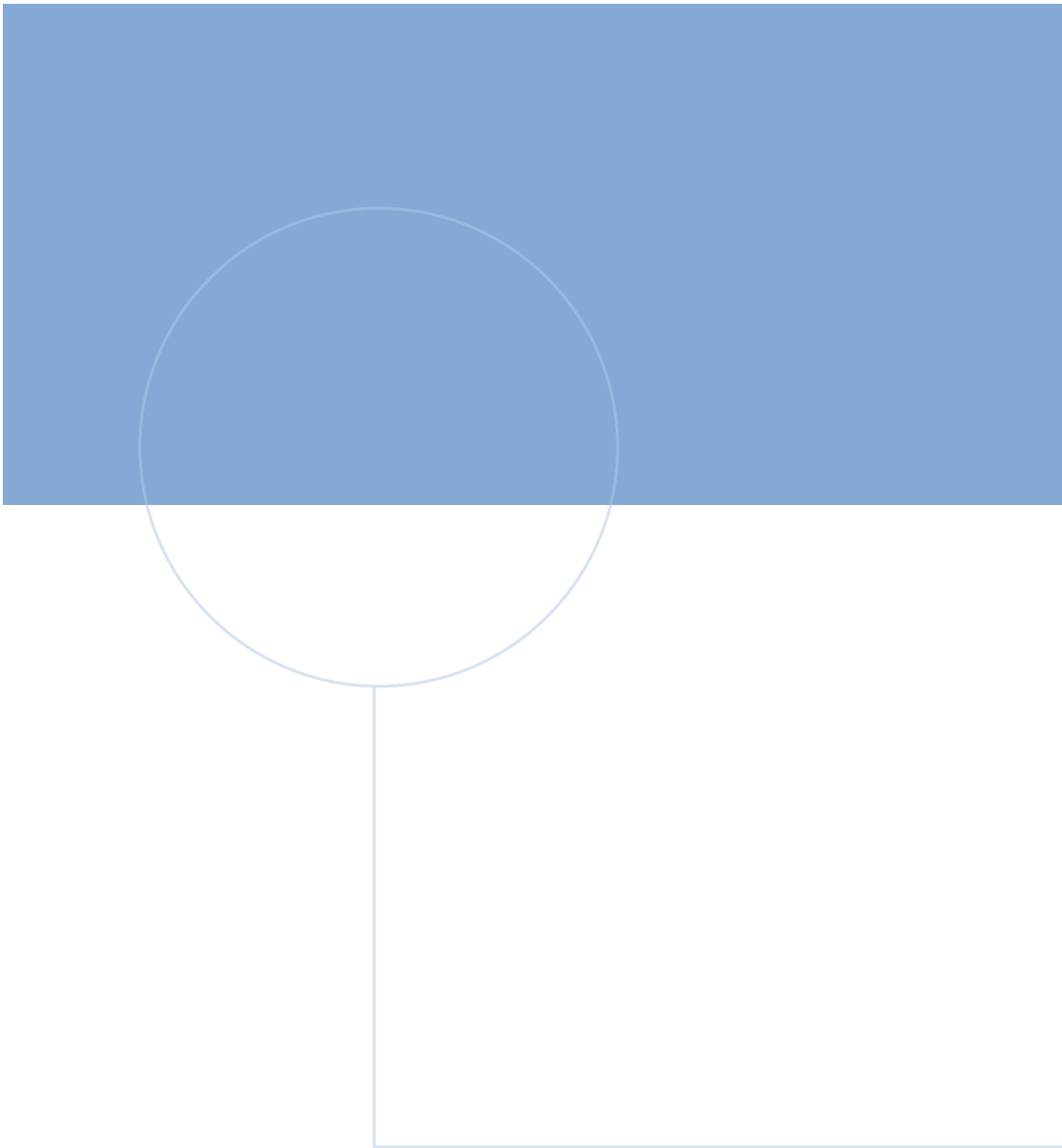

NTNU

Norwegian University of
Science and Technology